AD_____

Award Number: W81XWH-07-1-0058

TITLE: Cone-Beam Computed Tomography for Image-Guided Radiation Therapy of Prostate Cancer

PRINCIPAL INVESTIGATOR: Seungryong Cho

CONTRACTING ORGANIZATION: The University of Chicago,
Chicago, IL 60637

REPORT DATE: January 2010

TYPE OF REPORT: Annual Summary

PREPARED FOR: U.S. Army Medical Research and Materiel Command
Fort Detrick, Maryland 21702-5012

DISTRIBUTION STATEMENT:

x Approved for public release; distribution unlimited

# REPORT DOCUMENTATION PAGE

*Form Approved*
*OMB No. 0704-0188*



| 1. REPORT DATE *(DD-MM-YYYY)* | 2. REPORT TYPE | 3. DATES COVERED *(From - To)* |
|---|---|---|
| 01-01-2010 | Annual Summary | 11 Dec 2006 – 11 Dec 2009 |

**4. TITLE AND SUBTITLE**

Cone-Beam Computed Tomography for Image-Guided Radiation Therapy of Prostate Cancer

**5a. CONTRACT NUMBER**

**5b. GRANT NUMBER**
W81XWH-07-1-0058

**5c. PROGRAM ELEMENT NUMBER**

**6. AUTHOR(S)**

Seungryong Cho

**5d. PROJECT NUMBER**

**5e. TASK NUMBER**

**5f. WORK UNIT NUMBER**

**7. PERFORMING ORGANIZATION NAME(S) AND ADDRESS(ES)**

The University of Chicago

Chicago, IL 60637

**8. PERFORMING ORGANIZATION REPORT NUMBER**

**9. SPONSORING / MONITORING AGENCY NAME(S) AND ADDRESS(ES)**
U.S. Army Medical Research and Materiel Command
Fort Detrick, Maryland 21702-5012

**10. SPONSOR/MONITOR'S ACRONYM(S)**

**11. SPONSOR/MONITOR'S REPORT NUMBER(S)**

**12. DISTRIBUTION / AVAILABILITY STATEMENT**

Approved for public release; distribution unlimited

**13. SUPPLEMENTARY NOTES**

**14. ABSTRACT**

The success of modern radiation therapy such as intensity-modulated radiation therapy (IMRT) or conformal radiation therapy (CRT) is heavily reliant on accurate image guidance in prostate cancer treatment. Cone-beam computed tomography (CBCT) is becoming one of the dominant imaging modalities for image-guidance partly because of its rich image information and its ease of use. However, current technology based on the Feldkamp-Davis-Kress (FDK) algorithm for image reconstruction from a circular scanning trajectory does have more room to improve in terms of image quality and accuracy. In addition, the imaging radiation dose is one of the key issues. This is of paramount importance especially in repeated scans during the treatment process to adapt treatment plans to changes in prostate over time. The overall objective of this project is to investigate and develop innovative CBCT scanning methods and corresponding image reconstruction algorithms that can increase the accuracy of the images of the patient's prostate and/or reduce patient dose from CBCT. Reverse helical CBCT has been proposed, and image reconstruction algorithms for the reverse helical scan have been developed and investigated. Region-of-interest imaging methods based on the chord-based reconstruction algorithm have been explored and applied to CBCT. A few-view CBCT approach based on iterative reconstruction algorithms has also been studied.

**5. SUBJECT TERMS**
cone-beam computed tomography, image-guided radiation therapy, region-of-interest, few-view

| 16. SECURITY CLASSIFICATION OF: | | | 17. LIMITATION OF ABSTRACT | 18. NUMBER OF PAGES | 19a. NAME OF RESPONSIBLE PERSON |
|---|---|---|---|---|---|
| a. REPORT | b. ABSTRACT | c. THIS PAGE | | | USAMRMC |
| U | U | U | UU | 45 | 19b. TELEPHONE NUMBER *(include area code)* |

## Table of Contents

## INTRODUCTION

The success of modern radiation therapy such as intensity-modulated radiation therapy (IMRT) or conformal radiation therapy (CRT) is heavily reliant on accurate image guidance in prostate cancer treatment [1]. Cone-beam computed tomography (CBCT) is becoming one of the dominant imaging modalities for image-guidance partly because of its rich image information and its ease of use. However, current technology based on the Feldkamp-Davis-Kress (FDK) algorithm for image reconstruction from a circular scanning trajectory does have more room to improve in terms of image quality and accuracy [2], although it is often acceptable for certain image-guidance tasks. In addition, the imaging radiation dose is one of the key issues; it has to be minimized or optimized for eventual improvement of radiation therapy via more frequent use of CBCT imaging [3]. This is of paramount importance especially in repeated scans during the treatment process to adapt treatment plans to changes in prostate over time. Recent progress in image reconstruction algorithm development for CBCT offers the potential for innovations in CBCT for image-guided radiation therapy (IGRT). The overall objective of this project is to investigate and develop innovative CBCT scanning methods and corresponding image reconstruction algorithms that can increase the accuracy of the images of the patient's prostate and/or reduce patient dose from CBCT. Reverse helical CBCT has been proposed, and image reconstruction algorithms for the reverse helical scan have been developed and investigated. Region-of-interest imaging methods based on the chord-based reconstruction algorithm have been explored and applied to CBCT. A few-view CBCT approach based on iterative reconstruction algorithms has also been studied. This report summarizes the progress of this Predoctoral Traineeship Award project made by the recipient during the past three years.

# BODY

## 1 Training Accomplishments

At the time of this report, the recipient, Seungryong Cho, of the Predoctoral Traineeship Award has taken 22 out of 22 required courses towards his Ph.D. degree in medical physics. The courses include physics of medical imaging, physics of radiation therapy, mathematics for medical physicists, image guided radiation therapy, statistics, anatomy of the body, radiation biology and teaching assistantship.

## 2 Research Accomplishments

### 2.1 Investigation of reconstruction algorithms for reverse helical CBCT

Currently, a kV-CT imaging scanner mounted on LINAC treatment system acquires cone-beam data by use of a scanning configuration in which the x-ray source and the detector move along a circular trajectory, with the gantry making a single rotation and the patient couch stationary. The FDK algorithm and its variations have been proposed, and widely used in practice, for reconstructing approximate images from circular cone-beam data. However, due to data insufficiency, there may exist cone-beam image artifacts that include intensity drop, streak artifacts, and image deformation in reconstructed images. The image artifacts would become more serious when a larger cone-angle is used for acquiring data.

Helical scanning configuration has been used widely in diagnostic CT for acquiring data sufficient for exact image reconstruction over an extended volume. In image-guided radiation therapy (IGRT) and other applications of CBCT, it is difficult, if not impossible, to implement mechanically a multiple-turn helical trajectory on the imaging systems due to hardware constraints. However, imaging systems in these applications often allow for the implementation of a reverse helical trajectory in which the rotation direction changes between two turns as shown in Fig. 1. Image reconstruction algorithms have been investigated for this novel scanning configuration.

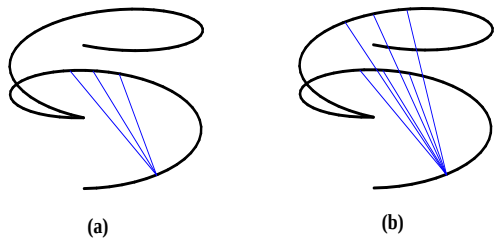

Figure 1: Illustration of chords (thin line segments) on a two-turn reverse helical trajectory (thick curve): one-turn chords (a), and two-turn chords (b).

#### 2.1.1 Chord-based BPF algorithm

The chord-based BPF algorithm decomposes the image into a number of chords, line segments that connect any two points on the source trajectory, and reconstructs the image on the chords which collectively cover the object [4]. Example chords are shown in Fig. 1 for a reverse helical trajectory. It can therefore easily be applied to a general source trajectory. In addition, the chord-based BPF algorithm is relatively robust against data truncation; for a given chord image, the projections of the chord need only be nontruncated over the scanning range that defines the chord. The flexibility of the algorithm and its robustness

against data truncation allow accurate region-of-interest imaging for general source trajectories . However, the algorithm cannot reconstruct images not on chords even though enough cone-beam data are provided for those chordless regions. The reverse helical trajectory is a good example that presents this limitation, and it is shown in Fig. 2 that there exists a middle chordless gap between two reconstructible regions by use of the chord-based BPF algorithm.

#### 2.1.2 Pack-Noo formula-based FBP algorithm

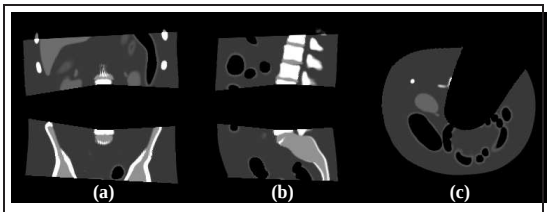

Figure 2: Reconstructed images of the NCAT phantom on (a) coronal, (b) sagittal, and (c) transverse slices by the chord-based BPF algorithm.

A shift-invariant filtered backprojection (FBP) algorithm that does not depend upon the chords has therefore been developed for volumetric image reconstruction in a reverse helical CBCT. Pack and Noo introduced a formula that relates a 3D inverse Radon transform with a filtered-backprojection of the cone-beam data, and successfully showed that the proposed formula can be used for image reconstruction from data that satisfy Tuy's condition, which is a data-sufficiency condition for exact image reconstruction in CBCT [5]. Based on the Pack-Noo formula, Yang *et al.* developed a useful approach for image reconstruction in CBCT with general, closed trajectories , which decomposes the object image into a number of polygon planes and reconstructs the polygon images through filtering the data and backprojecting the filtered data onto the polygon [6]. We made an extension to this approach for image reconstruction in CBCT with general, open trajectories such as reverse helix, and demonstrated successful reconstruction of images [7]. Since the Pack-Noo formula based algorithm does not require the existence of chords, the chordless gap region can be reconstructed by this algorithm. A paper on the developed FBP algorithm is published in Medical Physics as attached in Appendix A.

#### 2.1.3 BPF-FBP tandem algorithm

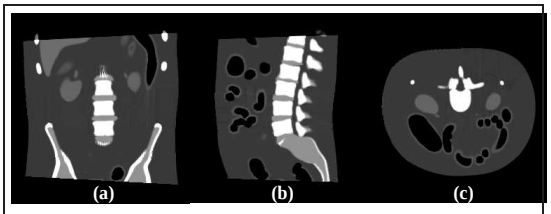

Figure 3: Reconstructed images of the NCAT phantom on (a) coronal, (b) sagittal, and (c) transverse slices by the BPF-FBP tandem algorithm.

However, the proposed FBP algorithm is not robust against data truncation within the polygon; only nontruncated object can be reconstructed exactly by the algorithm. In other words, it cannot handle a long object that extends beyond the reverse helix along the longitudinal direction. In practice, the imaging object is long enough that it frequently extends out of the polygon in reverse helical CBCT. Having seen cons and pros of the two algorithms - the chord-based BPF algorithm and the Pack-Noo formula-based algorithm - naturally motivated us to develop a hybrid approach that combines these strengths of each algorithm. A BPF-FBP tandem algorithm for image reconstruction in reverse helical CBCT has been developed [8]. The chord-based BPF algorithm reconstructs part of the volumetric image from the original cone-beam data first, and the chordless gap region is then reconstructed by the Pack-Noo formula-based FBP algorithm from the cone-beam data after subtracting the reprojection of the first reconstructed volumetric image. The NCAT

phantom images reconstructed by the tandem algorithm are shown in Fig. 3. The paper on this hybrid approach is published in Medical Physics as attached in Appendix B.

## 2.2 Investigation of ROI imaging in circular CBCT

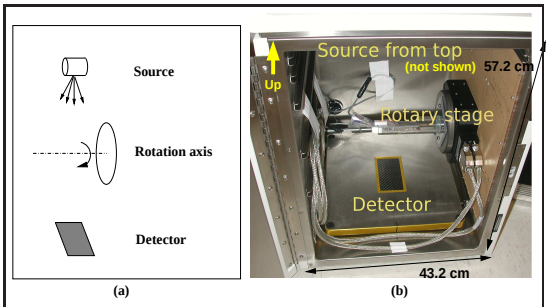


Figure 4: The prototype micro-CT system: (a) A schematic diagram. (b) The x-ray source is on the top, the detector is placed on the bottom, and the rotary stage is placed orthogonally to the beam.

ROI imaging in conjunction with the chord-based BPF algorithm has been applied to a circular cone-beam micro-CT for volumetric images of the ROI with a higher spatial resolution and at a reduced exposure to the imaged object. Although micro-CT is not directly related to radiation therapy, it is fundamentally similar to CBCT used for IGRT. A micro-CT system based on a flat panel detector (FPD) shares the physics of CBCT systems such as the Varian on-board imaging (OBI): the X-ray source irradiates in wide enough cone and fan angles to cover the entire FPD, the detector placed facing the X-ray source constructs a cone-beam geometry, and either the gantry mounted with source and detector or the object holder can rotate to achieve a circular scan.

An object-rotating micro-CT system offers much higher flexibility and better access to modifying or tailoring the system than does a clinical CBCT system. Therefore, a prototype micro-CT system has been developed for providing a testbed on which we can experimentally demonstrate the proposed algorithms and can perform a variety of preclinical, translational studies in addition [9].

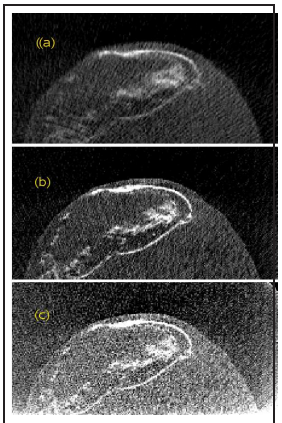


Figure 5: Slice-images of the mouse leg bearing osteosarcoma reconstructed (a) by the FDK algorithm from the complete data set with lower geometric magnification, (b) by the chord-based BPF algorithm and (c) by the FDK algorithm from the truncated data set with higher geometric magnification.

### 2.2.1 Development of a prototype micro-CT

The system consists of a microfocal X-ray source, an orthogonally-mounted rotary stage with object holder, and a CsI-coupled CMOS detector. The microfocal X-ray source (MX-20, Faxitron, USA), comprised of a tungsten anode with beryllium exit window, can be operated between 10-35 kV at a fixed tube current of 300 $\mu A$, and can yield a focal spot size of about 20 $\mu m$. The 14-bit digital camera (Bioptics, USA) consists of a CsI scintillator plate and a 2048 $\times$ 1024 array of CMOS thin-film transistors and photodiodes with a pixel size of about 50 $\mu m$. The Faxitron system was originally designed for specimen radiography and has been used to produce quality images of various samples including mammographic samples. The system has been successfully modified, in both hardware and software, into a prototype cone-beam micro-CT system. The rotary stage (ADRS-150, Aerotech, USA) can load upto about 10 kg weight along the radial direction and has an accuracy about 10 arc seconds. A picture of the system is shown in Fig. 4.

#### 2.2.2 ROI imaging of a mouse leg bearing osteosarcoma

We applied the chord-based BPF algorithm to reconstructing ROI images from truncated cone-beam data acquired with the micro-CT system. In particular, we demonstrated how the algorithm's capability of reconstructing ROI images from truncated data can be exploited to enhance the spatial resolution of the images. A uniform lucite phantom and a mouse with one leg bearing an osteosarcoma were used in the validation of the proposed method. We have shown that the chord-based BPF algorithm can reconstruct ROI images, from truncated data, with image quality comparable to that of the images reconstructed from nontruncated data. ROI imaging in conjunction with the chord-based algorithm can enhance image resolution, thereby improving image quality, and can reduce the imaging radiation dose to the object at the same time [10].

### 2.3 Investigation of IWROI imaging in circular CBCT

For imaging targets located deep within the body the ROI becomes an interior problem, for which no stable, accurate image reconstruction method exists. The local tomography method provides edge-enhanced images from ROI projection data, but this approach does not provide accurate image contrast information which is important in many applications including IGRT. We have developed an intensity-weighted region-of-interest (IWROI) imaging technique which can reduce the imaging radiation dose to structures away from the imaging target, while allowing solution of the reconstruction problem by using the chord-based BPF algorithm. We subdivide the reconstructed ROI into inner and outer regions, and illuminate the outer region with a filtered beam to decrease exposure during the scan. Our approach allows some types of data truncation without causing artifacts in the reconstructed ROI image and allows different exposure levels in two sub-ROIs from a single scan. We focused on circular CBCT, which is the dominant imaging modality employed in most radiation therapy systems, although the method can be extended to general scanning configurations such as the saddle trajectory.

Clinical feasibility of the IWROI imaging was demonstrated with the OBI system on a Trilogy linear accelerator (Varian Medical Systems) [11]. The OBI system is composed of an x-ray source and flat panel detector mounted on the accelerator gantry orthogonal to the treatment beam as shown in Fig. 6. A nonuniform filter is placed in the x-ray beam to create regions of two different beam intensities. In this manner, regions outside the target area can be given a reduced dose but still visualized with a lower contrast-to-noise-ratio (CNR). Physical factors such as scatter from the object and beam hardening due to the intensity-weighting filter have corrected for, and the effects of correction are demonstrated visually in Fig. 7 for a solid water phantom. Image artifacts due to transverse data truncation, which would have occurred in conventional reconstruction algorithms, are avoided and image noise levels of the low and high-intensity regions are well

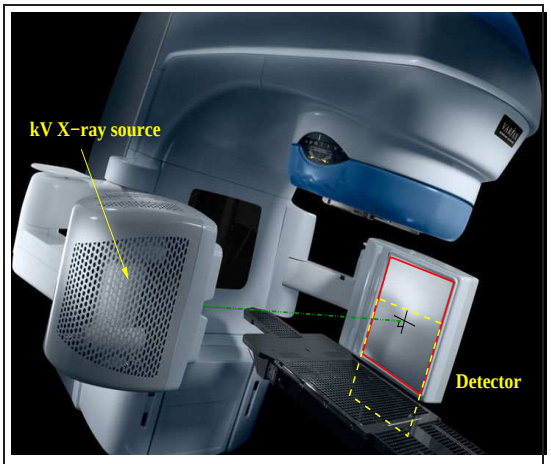

Figure 6: A picture of the Varian OBI system.

controlled by use of the chord-based BPF reconstruction algorithm. A preliminary measurement of dose reduction has been performed, and we believe the proposed IWROI technique can play an important role in prostate IGRT. The details of the work can be found in the attached paper, Appendix C.

### 2.4 Investigation of few-view CBCT for IGRT

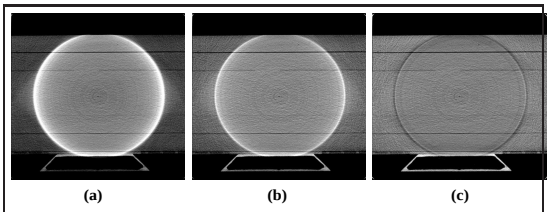


Figure 7: Transverse slice images of the reconstructed SW-phantom scanned with Cu1-filter are displayed; (a) No correction, (b) scatter correction, and (c) scatter + beam quality correction have been applied.

As another attempt to reduce patient dose, we have investigated a few-view CBCT for IGRT. One unique feature of CBCT for interfraction motion detection is the availability of prior anatomical images which are substantially unchanged. A prior image may be available from the previous fraction CBCT scan, or an initial CBCT set-up scan. These scans contain the same anatomical information as the current scan except for anatomical changes due to internal motion or patient weight gain/loss. However, a substantial portion of the image, particularly including bony structures and surrounding tissues, remains unchanged. We proposed an iterative algorithm for image reconstruction from a very limited number of projections in CBCT, which is based on minimization of the image total-variation (TV) subject to the constraints of data fidelity and positivity and that utilizes information available from a prior image.

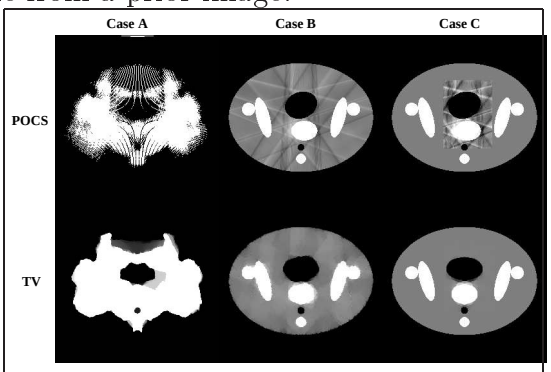


Figure 8: Reconstructed images of the pelvis phantom. No prior image information was used in case A (left). Case B (middle) represents the case using the prior image as an initial guess, but no mask; and case C (right) represents the case using both prior image and mask.

We have previously proposed a TV algorithm utilizing prior image with internal motion as an initial guess in few-view fan-beam CT, and successfully demonstrated that the number of views for image reconstruction can be reduced from that needed in the TV algorithm without prior in the numerical study (roughly speaking, from 20 views to 10 views) [12]. Using the prior image as an initial image estimate in the iterative process is thought to help find the true minimum TV image that meets the data fidelity constraint, whereas a local minimum may be found when no prior image information is used. However, it was observed that the unchanged portion of the prior image, which is controlled in the numerical study, is vulnerable to change as the iteration steps advance and may degrade when the amount of projection data is extremely limited (e.g. five views). In the modified work, we mask the image region that is unchanged from the prior image so that the masked region is not influenced by the updates during iterative steps [13]. We demonstrated in numerical simulations that successful image reconstruction can be realized from five views as shown in Fig. 8. The preliminary study has been published in SPIE Medical Imaging Conference Proceedings, 2009.

### 2.5 Investigation of dual-energy imaging

We investigated the feasibility of dual-energy method for image contrast enhancement in small animal studies using a low kV x-ray radiographic system as a preliminary study of dual-energy CBCT for IGRT. A robust method for x-ray spectrum estimation from transmission measurements, based on expectation-maximization (EM) method, was applied to an x-ray specimen radiographic system for dual energy imaging of a mouse [14]. From transmission measurements of two known attenuators at two different x-ray tube voltages, the x-ray energy spectra were reconstructed using the EM-based method. From the spectra information thus obtained, the transmission data for bone and soft tissue in terms of various thicknesses were generated. Two polynomial functions of transmission data were then sought for to fit the inverted thicknesses of bone and soft-tissue. Scatters in cone-beam projection data acquired at two x-ray energies were corrected for. From the scatter-corrected data, a bone thickness map was separated from a soft-tissue thickness map by use of the polynomial functions as shown in Fig. 9.

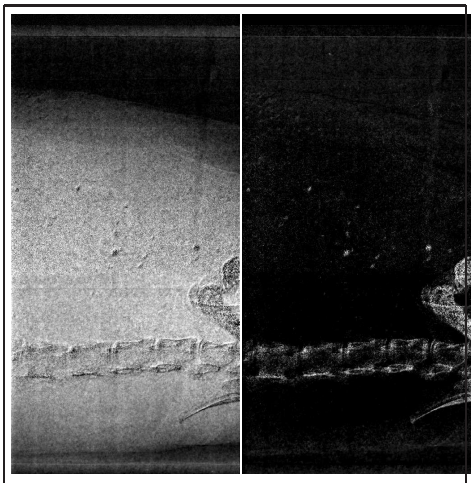

Figure 9: Tissue thickness map (left) and bone thickness map (right) calculated from the transmission data.

## KEY RESEARCH ACCOMPLISHMENTS

- We have proposed a novel image acquisition geometry of reverse helix for CBCT imagers mounted on LINAC treatment systems used for prostate cancer IGRT.
- We have developed an exact FBP-type image reconstruction algorithm for a short object within the reverse helix.
- We have proposed a hybrid approach for image reconstruction of a long object in reverse helical CBCT.
- We have developed a BPF-FBP tandem algorithm for image reconstruction of a long object in the reverse helical CBCT.
- We have developed a prototype micro-CT system that can be used as a testbed for CBCT experiments.
- We have developed an ROI imaging scheme for a mouse leg bearing osteosarcoma, and successfully reconstructed ROI images from truncated data.
- We have shown the ROI imaging method can be utilized for obtaining higher spatial resolution of an ROI image.
- We have developed an IWROI method, illuminating an outer ROI around the target (prostate) with a reduced fluence, thereby permitting accurate reconstruction with dose savings.
- We have demonstrated the feasibility of the IWROI imaging for prostate cancer CBCT using the OBI system on a Trilogy linear accelerator (Varian Medical Systems).
- We have developed correction methods for physical factors such as scatter and beam-hardening in the IWROI imaging.
- We have conducted a preliminary measurement of dose reduction via IWROI imaging and reported substantial reduction of imaging radiation dose.
- We have developed a few-view CBCT scheme based on an algorithm of total-variation minimization for image reconstruction with the use of prior image information.
- We have performed a preliminary, numerical study of a prior-image-based few-view CBCT for prostate cancer IGRT based on TV algorithm.
- We have developed an x-ray spectrum estimation method from transmission measurements based on an EM algorithm.
- We have developed a dual-energy radiography technique to decompose an image into bone map and soft-tissue map, based on which 3D dual-energy imaging can be constructed.

## REPORTABLE OUTCOMES

### Peer-reviewed Journal Articles

1. **S. Cho**, E. Y. Sidky, J. Bian, and X. Pan, "Dual-energy technique at low tube voltages for small animal imaging", Tsinghua Sci. Technol., (in press), 2010.
2. D. Xia, **S. Cho**, and X. Pan, "Backprojection-filtration reconstruction without invoking a spatially varying weighting factor", Med. Phys., (accepted), 2010.
3. **S. Cho**, D. Xia, C. A. Pelizzari, and X. Pan, "A BPF-FBP tandem algorithm for image reconstruction in reverse helical cone-beam computed tomography", Med. Phys., 37, 32-39, 2010.
4. D. Xia, **S. Cho**, and X. Pan, "Image reconstruction in reduced circular sinusoidal cone-beam CT", J. X-ray Sci. Tech., 17, 189-205, 2009.
5. **S. Cho**, E. Pearson, C. A. Pelizzari, and X. Pan, "Region-of-interest imaging with intensity-weighting in circular cone-beam CT for image-guided radiation therapy", Med. Phys., 36, 1184-1192, 2009.
6. **S. Cho**, D. Xia, C. A. Pelizzari, and X. Pan, "Exact reconstruction of volumetric images in reverse helical cone-beam CT", Med. Phys., 35, 3030-3040, 2008.
7. **S. Cho**, J. Bian, C. A. Pelizzari, C.-T. Chen, T.-C. He, and X. Pan, "Region-of-interest image reconstruction in circular cone-beam microCT", Med. Phys., 34, 4923-4933, 2007.

### Conference Proceeding Articles

1. **S. Cho**, D. Xia, E. Pearson, C. A. Pelizzari, and X. Pan, "Half-fan-based region-ofinterest imaging in circular cone-beam CT for radiation therapy", Proc. of 2009 International Meeting on Fully 3D Image Reconstruction in Radiology and Nuclear Medicine, 385-388, 2009.
2. X. Han, **S. Cho**, J. Bian, E. Pearson, E. Y. Sidky, C. A. Pelizzari, and X. Pan, "Low-dose kilovoltage cone-beam CT imaging for image-guided radiation therapy: a feasibility study", Proc. of 2009 International Meeting on Fully 3D Image Reconstruction in Radiology and Nuclear Medicine, 389-393, 2009.
3. D. Xia, **S. Cho**, and X. Pan, "Backprojection filtration algorithm with improved noise property for a circular cone-beam CT", Proc. of 2009 International Meeting on Fully 3D Image Reconstruction in Radiology and Nuclear Medicine, 170-173, 2009.
4. **S. Cho**, D. Xia, C. A. Pelizzari, and X. Pan, "Exact image reconstruction in reverse helical cone-beam CT", Proc. of 2007 International Meeting on Fully 3D Image Reconstruction in Radiology and Nuclear Medicine, 84-87, 2007.
5. D. Xia, **S. Cho**, and X. Pan, "Image reconstruction for a reduced scan in circular sinusoidal cone-beam CT", Proc. of 2007 International Meeting on Fully 3D Image Reconstruction in Radiology and Nuclear Medicine, 213-216, 2007.

6. **S. Cho**, E. Pearson, E. Sidky, J. Bian, C. A. Pelizzari, and X. Pan, "Prior-imagebased few-view cone-beam CT for applications to daily scans in image-guided radiation therapy: Preliminary study", Proc. SPIE, Vol. 7258, 7258-65, 2009.

7. **S. Cho**, E. Pearson, C. A. Pelizzari, and X. Pan, "Noise analysis in intensity-weighted region-of-interest imaging for cone-beam CT", Proc. SPIE, Vol. 7258, 7258-06, 2009.

8. D. Xia, **S. Cho**, J. Bian, E. Sidky, C. A. Pelizzari, and X. Pan, "Tomosynthesis with source distributions over a surface", Proc. SPIE, Vol. 6913, 69132A, 2008.

9. **S. Cho**, E. Sidky, C. A. Pelizzari, and X. Pan, "A preliminary investigation of using prior information for potentially improving image reconstruction in few-view CT", Proc. SPIE, Vol. 6913, 69132C, 2008.

10. **S. Cho**, E. Pearson, D. Xia, X. Han, C. A. Pelizzari, and X. Pan, "A preliminary study of intensity-weighted ROI imaging in cone-beam CT", Proc. SPIE, Vol. 6913, 691325, 2008.

11. **S. Cho**, D. Xia, C. A. Pelizzari, and X. Pan, "Cone-beam CT with a modified reverse helical trajectory for long object problem", IEEE Medical Imaging Conference, M18-282, 2007.

12. D. Xia, **Seungryong Cho**, and Xiaochuan Pan, "Extended reconstructible volume in reduced saddle scan", IEEE Medical Imaging Conference, M04-5, 2007.

13. Dan Xia, **S. Cho**, and X. Pan, "Image noise properties in circular sinusoid cone-beam CT", IEEE Medical Imaging Conference, M13-285, 2007.

14. X. Zhao, J. Bian, E. Y. Sidky, **S. Cho**, P. Zhang, and X. Pan, "GPU-Based 3D Cone-Beam CT Image Reconstruction: Application to Micro-CT", IEEE Medical Imaging Conference, M19-287, 2007.

### Conference Presentations and Abstracts

1. E. Pearson, **S. Cho**, X. Pan, and C. A. Pelizzari, "Comparison of achievable dose reduction in CBCT for the prostate using intensity-weighted and conformal region of interest imaging techniques", ASTRO, Chicago, IL, 2009.

2. **S. Cho**, D. Xia, C. A. Pelizzari, and X. Pan, "Utilization of two analytic algorithms for image reconstruction in cone-beam CT", IEEE Medical Imaging Conference, M05-22, 2009.

3. X. Han, J. Bian, E. Pearson, **S. Cho**, E. Y. Sidky, C. A. Pelizzari, and X. Pan, "Low-dose kilo-voltage cone-beam CT image reconstruction by constrained total-variation minimization: experience with clinical data", IEEE Medical Imaging Conference, M12-5, 2009.

4. **S. Cho**, E. Pearson, C. A. Pelizzari, and X. Pan, "Image artifacts caused by the extra focal spot of an x-ray tube in cone-beam computed tomography", AAPM, Houston, TX, 2008.

5. E. Pearson, **S. Cho**, X. Pan, and C. A. Pelizzari, "Dose reduction in CBCT via intensity-weighted region-of-interest imaging", AAPM, Houston, TX, 2008.

6. E. Pearson, **S. Cho**, X. Pan, and C. A. Pelizzari, "Region-of-interest imaging for cone-beam CT in radiation therapy", Varian Research Partnership Symposium, Austin, TX, 2008.

7. **S. Cho**, D. Xia, C. A. Pelizzari, and X. Pan, "Reverse helical cone-beam CT and its application to image-guided radiation therapy", RSNA, Chicago, IL, 2007.

8. **S. Cho**, D. Xia, C. A. Pelizzari, and X. Pan, "Exact image reconstruction in reverse helical cone-beam CT for radiation therapy", AAPM, Minneapolis, MN, 2007.

9. X. Han, **S. Cho**, W. Song, T. He, and X. Pan, "Micro-CT imaging and quantitative characterization of bone morphogenetic protein regulated differentiation of mesenhcymal stem cells", AAPM, Minneapolis, MN, 2007.

10. **S. Cho**, D. Xia, C. A. Pelizzari, and X. Pan, "Exact image reconstruction in reverse helical cone-beam CT for radiation therapy", AAPM Midwest Chapter Meeting, Oak Lawn, Apr. 21, 2007.

**Honors and Awards**

- The Carl J. Vyborny Journal Club Award, Graduate Programs in Medical Physics, The University of Chicago, 2008.
- Paul C. Hodges Research Award, Department of Radiology, The University of Chicago, 2008.
- Young Investigator Award (2nd place), AAPM Midwest Chapter Meeting, 2007.
- Student Travel Grant Award, SPIE Medical Imaging Conference, 2007.
- Student Trainee Award, IEEE NSS-MIC, 2007, 2009.

## CONCLUSIONS

The recipient of the Predoctoral Traineeship Award has finished the required courses towards his Ph.D. degree. These trainings have proven useful for the recipient to achieve the proposed research goals.

During the funded years, we have investigated innovative approaches in CBCT for IGRT that can increase the accuracy of the reconstructed images and/or reduce radiation dose to a prostate cancer patient. A BPF-FBP tandem image reconstruction algorithm has been developed for prostate IGRT using a reverse helical CBCT scan to improve image accuracy and quality. ROI and IWROI imaging methods have been developed for sparing imaging radiation dose to the surrounding tissues and overall dose to the patient as well while maintaining quality images of the imaging target. Clinical feasibility of the IWROI imaging method has been successfully demonstrated. A prior-image-based few-view CBCT technique has been proposed and an iterative algorithm for image reconstruction has been developed. The preliminary results of a numerical study suggest its potential usefulness in prostate IGRT. Dual-energy imaging approach has been investigated in a micro-CT system for potential extension to CBCT in prostate IGRT.

Overall, we have achieved the goals for the project, and will continue further research on a thorough evaluation of dose reduction via IWROI imaging, an experimental demonstration of the feasibility of the prior-image-based few-view CBCT, and experimental implementation of the reverse helical CBCT.

## REFERENCES


1. D. Verellen, M. D. Ridder, N. Linthout, K. Tournel, G. Soete, and G. Storme: Innovations in image-guided radiotherapy, Nature Reviews Cancer, 7, 949-960, 2007.

2. Y. Zou, A. A. Zamyatin, B. S. Chiang, and M. D. Silver: Reduction of streak artifacts in circular cone beam CT using scanograms, Proc. IEEE MIC, M18-294, 2007

3. M. J. Murphy, J. Balter, S. Balter, J. A. BenComo, I. J. Das, S. B. Jiang, C. -M. Ma, G. H. Olivera, R. F. Rodebaugh, K. J. Ruchala, H. Shirato, and F. -F. Yin: The management of imaging dose during image-guided radiotherapy: Report of the AAPM Task Group 75 , Med. Phys., 34, 4041-4063, 2007.

4. Y. Zou and X. Pan: Exact image reconstruction on PI-line from minimum data in helical cone-beam CT, Phys. Med. Biol., 49, 941-959, 2004.

5. J. D. Pack and F. Noo: Cone-beam reconstruction using 1D filtering along the projection of M-lines, Inv. Prob., 21, 1105-1120, 2005.

6. H. Yang, M. Li, K. Koizumi, and H. Kudo: Exact cone beam reconstruction for a saddle trajectory, Phys. Med. Biol., 51, 1157-1172, 2006.

7. S. Cho, D. Xia, C. A. Pelizzari, and X. Pan: Exact reconstruction of volumetric images in reverse helical cone-beam CT, Med. Phys., 35, 3030-3040, 2008.

8. S. Cho, D. Xia, C. A. Pelizzari, and X. Pan: A BPF-FBP tandem algorithm for image reconstruction in reverse helical cone-beam computed tomography, Med. Phys., 37, 32-39, 2010.

9. S. Cho, J. Bian, C. A. Pelizzari, J. S. Souris, C.-T. Chen, and X. Pan: Performance evaluation of a prototype micro-CT system, Proc. IEEE MIC , M14-183, 2006.

10. S. Cho, J. Bian, C. A. Pelizzari, C.-T. Chen, T.-C. He, and X. Pan: Region-of-interest image reconstruction in circular cone-beam microCT, Med. Phys., 34, 4923-4933, 2007.

11. S. Cho, E. Pearson, C. A. Pelizzari, and X. Pan: Region-of-interest imaging with intensity-weighting in circular cone-beam CT for image-guided radiation therapy, Med. Phys. 36, 1184-1192, 2009.

12. S. Cho, E. Pearson, E. Sidky, J. Bian, C. A. Pelizzari, X. Pan: Prior-image-based few-view cone-beam CT for applications to daily scan in image-guided radiation therapy: Preliminary study, Proc. SPIE, Vol. 7258, 7258-65, 2009.

13. S. Cho, E. Y. Sidky, C. A. Pelizzari, and X. Pan: Few-view cone-beam computed tomography for image-guided radiation therapy , Proc. SPIE, Vol. 6913, 69132C, 2008.

14. S. Cho, E. Y. Sidky, J. Bian, X. Pan: Dual-energy technique at low tube voltages for small animal imaging, Tsinghua Sci. Technol., 15, (in press), 2010.

## APPENDICES

- Appendix A: S. Cho, D. Xia, C. A. Pelizzari, and X. Pan: Exact reconstruction of volumetric images in reverse helical cone-beam CT, Med. Phys., 35, 3030-3040, 2008.
- Appendix B: S. Cho, D. Xia, C. A. Pelizzari, and X. Pan: A BPF-FBP tandem algorithm for image reconstruction in reverse helical cone-beam computed tomography, Med. Phys., 38, 32-39, 2010.
- Appendix C: S. Cho, E. Pearson, C. A. Pelizzari, and X. Pan: Region-of-interest imaging with intensity-weighting in circular cone-beam CT for image-guided radiation therapy, Med. Phys. 36, 1184-1192, 2009.

# Exact reconstruction of volumetric images in reverse helical cone-beam CT

Seungryong Cho
*Department of Radiology and Department of Radiation and Cellular Oncology, University of Chicago, Illinois 60637*

Dan Xia
*Department of Radiology, University of Chicago, Chicago, Illinois 60637*

Charles A. Pelizzari
*Department of Radiation and Cellular Oncology, University of Chicago, Chicago, Illinois 60637*

Xiaochuan Pan[a)]
*Department of Radiology, University of Chicago, Chicago, Illinois 60637*

(Received 26 December 2007; revised 22 April 2008; accepted for publication 23 April 2008; published 12 June 2008)

Helical scanning configuration has been used widely in diagnostic cone-beam computed tomography (CBCT) for acquiring data sufficient for exact image reconstruction over an extended volume. In image-guided radiation therapy (IGRT) and other applications of CBCT, it can be difficult, if not impossible, to implement mechanically a multiple-turn helical trajectory on the imaging systems due to hardware constraints. However, imaging systems in these applications often allow for the implementation of a reverse helical trajectory in which the rotation direction changes between two consecutive turns. Because the reverse helical trajectory satisfies Tuy's condition, when projections of the imaged object are nontruncated, it yields data sufficient for exact image reconstruction within the reverse helix volume. The recently developed chord-based algorithms such as the backprojection filtration (BPF) algorithm can readily be applied to reconstructing images on chords of a reverse helical trajectory, and they can thus reconstruct an image within a volume covered by the chords. Conversely, the chord-based algorithms cannot reconstruct images within regions that are not intersected by chords. In a reverse helix volume, as shown below, chordless regions exist in which no images can thus be reconstructed by use of the chord-based algorithms. In this work, based upon Pack–Noo's formula, a shift-invariant filtered backprojection (FBP) algorithm is derived for exact image reconstruction within the reverse helix volume, including the chordless region. Numerical studies have also been conducted to demonstrate the chordless region in a reverse helix volume and to validate the FBP algorithm for image reconstruction within the chordless region. Results of the numerical studies confirm that the FBP algorithm can exactly reconstruct an image within the entire reverse helix volume, including the chordless region. It is relatively straightforward to extend the FBP algorithm to reconstruct images for general trajectories, including reverse helical trajectories with variable pitch, tilted axis, and/or additional segments between turns.  [DOI: 10.1118/1.2936219]

Key words: cone-beam computed tomography, reconstruction, reverse helical, filtered backprojection, image-guided radiation therapy

## I. INTRODUCTION

Computed tomography (CT) is used widely as one of the leading imaging modalities in image-guided radiation therapy (IGRT). In the last few years, cone-beam CT (CBCT) with a KV source that is mounted on the rotation gantry of a linear accelerator (LINAC) treatment system has become commercially available.[1–3] Integration of such a KV-CT imaging component into the LINAC system allows the KV-imaging and MV-treatment processes to share identical spatial, and temporal information about the treated patient. Currently, a KV-CT imaging scanner mounted on LINAC treatment system acquires cone-beam data by use of a scanning configuration in which the x-ray source and the detector move along a circular trajectory, largely because the mechanical implementation of a circular configuration is relatively easy. The FDK algorithm[4] and its variations have been proposed, and widely used in practice, for reconstructing approximate images from circular cone-beam data. However, due to data insufficiency, there may exist cone-beam image artifacts that include intensity drop, streak artifacts, and image deformation in reconstructed images.[5,6] The image artifacts would become more serious when a larger cone angle is used for acquiring data.

The helical source trajectory has become a standard scanning configuration in diagnostic CT because it can collect cone-beam data sufficient for exact reconstruction of volume images. Diagnostic CT achieves an extended longitudinal coverage by use of the slip-ring technology, which allows the x-ray source and the detector to rotate multiple turns continuously in one direction, while the patient couch is translated at a constant speed along one direction, thus forming a

multiple-turn helical source trajectory. The LINAC-mounted KV cone-beam CT, however, can rotate only one turn in either direction, and must reverse rotation direction after each turn. Therefore, the LINAC-mounted KV cone-beam CT imager can achieve only a one-turn helical source trajectory without altering the couch motion mode. It is expected that certain image-guided radiation therapy (IGRT) applications based on cone-beam CT images may benefit from an extended volume coverage of the patient.[7] Although single-turn helical trajectory offers some extension of the imaged volume, it may be desirable to achieve an extended longitudinal coverage beyond that of a one-turn helical trajectory. One natural way to extend the longitudinal coverage is that the couch is translated continuously along one direction while the LINAC gantry reverses its rotation direction after each turn, thus resulting in a multiple-turn reverse helical trajectory.

In this work, we investigate image reconstruction from cone-beam data acquired with reverse helical trajectories. In the last several years, significant advances have been made in algorithm development for accurate image reconstruction in helical CBCT, including Katsevich's filtered-backprojection-type algorithm and the chord-based algorithms.[8–10] These algorithms have also been extended to the algorithms for general source trajectories.[11–15] We first apply, in this work, the recently developed chord-based algorithm[10,13] to reconstructing images because they are directly applicable to general continuous trajectories including reverse helical trajectories. A chord is defined as a line segment connecting any two points on a continuous source trajectory; and chord-based algorithms reconstruct volume images through reconstructing images on all of the chords that intersect the volume. Because any selected volume enclosed by a conventional helical trajectory used in diagnostic CT is covered completely by chords,[16] chord-based algorithms can reconstruct images within the selected volume for a conventional helical trajectory.

As will be shown below, however, some portions of the reverse helix volume are not intersected by any chords, thus forming chordless regions in which images cannot be reconstructed by use of the chord-based algorithms. Therefore, the focus of the work is at developing a shift-invariant filtered backprojection (FBP) reconstruction algorithm for exactly reconstructing images within the entire reverse helix volume based upon Pack–Noo's formula.[17,18] We have conducted a study to analyze and demonstrate numerically the chordless region in a reverse helix volume that cannot be reconstructed by use of the chord-based algorithm. Additional numerical studies were conducted to validate the proposed FBP algorithm for image reconstruction within the chordless region. Results of the numerical studies confirm that, unlike the chord-based backprojection filtration (BPF) algorithm that can yield only an incomplete volume image, the proposed FBP algorithm can exactly reconstruct an image within the reverse helix volume. It is worthwhile to note, however, that the proposed FBP algorithm cannot be used directly for long object scan, because the algorithm involves data filtering along the longitudinal direction, along which the projection data may contain data truncation. However, it may be possible to address the long object problem by combining the chord-based BPF and the proposed FBP algorithms. It is relatively straightforward to extend the proposed FBP algorithm to reconstruct images for general trajectories, including reverse helical trajectories with variable pitch, tilted axis, and/or additional line segments between turns.

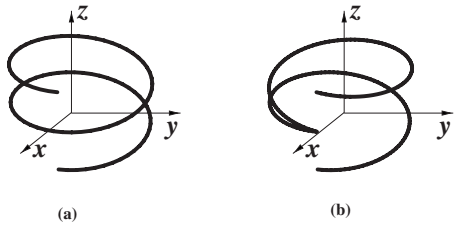


FIG. 1. A two-turn conventional helical trajectory (a) and a two-turn reverse helical trajectory (b) in the coordinate system $\{x,y,z\}$ that is fixed on the imaged object.

## II. A REVERSE HELICAL TRAJECTORY

The conventional helical and reverse helical trajectories can be specified by the rotation angle $\lambda$ of the source. For comparison, we give below the mathematical expressions for the two trajectories in the coordinate system that is fixed on the imaged object. For a conventional helical trajectory $\vec{r}_0(\lambda)$, it can be expressed as

$$\vec{r}_0(\lambda)=\left(R\cos\lambda,R\sin\lambda,\frac{h}{2\pi}\right),\quad \lambda\in[\lambda_s,\lambda_e], \tag{1}$$

where $R$ denotes the distance from the source to the rotation axis, $h$ the helical pitch, and $\lambda_s$ and $\lambda_e$ the starting and ending angle of the helical trajectory. In Fig. 1(a), we display a two-turn conventional helical trajectory specified by $\lambda\in[\lambda_s,\lambda_e]=[-2\pi,2\pi]$. In contrast, the reverse helical trajectory $\vec{r}_0(\lambda)$ can be written as

$$\vec{r}_0(\lambda)=\left(R\cos((-1)^n\lambda),R\sin((-1)^n\lambda),\frac{h}{2\pi}\lambda\right),$$

$$\lambda\in[\lambda_s,\lambda_e], \tag{2}$$

where integer $n$ indicates the $n$th turn, and it can be written in terms of a floor function "⌊⌋" as

$$n=\left\lfloor\frac{\lambda}{2\pi}\right\rfloor+1. \tag{3}$$

Without loss of generality, we have assumed that the turn with $n=0$ in the reverse helical trajectory is a turn in the conventional helical trajectory. For example, as shown in Fig. 1, for a two-turn reverse helical trajectory specified by $\lambda\in[\lambda_s,\lambda_e]=[-2\pi,2\pi]$, we have

$$\vec{r}_0(\lambda)=\left(R\cos\lambda,R\sin\lambda,\frac{h}{2\pi}\lambda\right),\quad \lambda\in[-2\pi,0)$$

$$\vec{r}_0(\lambda)=\left(R\cos(-\lambda),R\sin(-\lambda),\frac{h}{2\pi}\lambda\right),\quad \lambda\in[0,2\pi]. \tag{4}$$

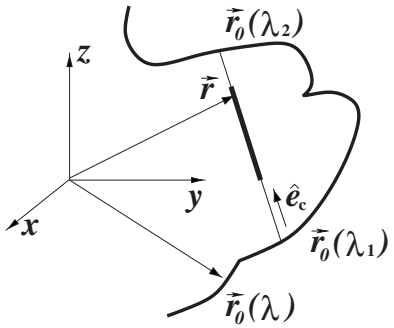


FIG. 2. Illustration of a chord (thin line segment) specified by $\lambda_1$ and $\lambda_2$ for a general, continuous trajectory. The direction of the chord is $\hat{e}_c$. The thick line segment on the chord indicates the support of the object.

Let $f(\vec{r})$ be an object function with a support that is contained completely within the volume enclosed by a reverse helical trajectory. The cone-beam projection from the source point $\vec{r}_0(\lambda)$ can be written as

$$g(\lambda,\hat{\theta}) = \int_0^\infty dt f(\vec{r}_0(\lambda) + t\hat{\theta}), \tag{5}$$

where $\hat{\theta}$ denotes the direction of x-ray transform of $f(\vec{r})$ from $\vec{r}_0(\lambda)$. The task of image reconstruction is to recover $f(\vec{r})$ from the cone-beam projection data acquired with a reverse helical trajectory $\vec{r}_0(\lambda)$ specified in Eq. (2).

## III. CHORD-BASED ALGORITHM FOR REVERSE HELICAL TRAJECTORIES

A chord of a continuous trajectory is defined as a line segment connecting any two points on the trajectory. If a volume is covered completely by chords, the image within the volume can be obtained through reconstructing images on all of the chords by use of the chord-based algorithms. Although the chord-based algorithms can have the forms of backprojection filtration (BPF)[10] and filtered backprojection (FBP),[19] we focus only on image reconstruction for a reverse helical trajectory by using the chord-based BPF algorithm in this section. Similar results can be obtained by use of the chord-based FBP algorithms.

### III.A. Chord-based BPF algorithm

We consider a chord specified by $\lambda_1$ and $\lambda_2$ on a given source trajectory $\vec{r}_0(\lambda)$. Let

$$\hat{e}_c = \frac{\vec{r}_0(\lambda_2) - \vec{r}_0(\lambda_1)}{\|\vec{r}_0(\lambda_2) - \vec{r}_0(\lambda_1)\|} \tag{6}$$

denote the direction of the chord, as shown in Fig. 2. Also, we use $x_c$ to indicate the coordinate of a point on the chord. It can be shown that the fixed coordinate and the chord coordinate of the point are related through

$$\vec{r} = \frac{1}{2}[\vec{r}_0(\lambda_1) + \vec{r}_0(\lambda_2)] + x_c\hat{e}_c, \quad x_c \in [-l,l], \tag{7}$$

where $l = 1/2\|\vec{r}_0(\lambda_2) - \vec{r}_0(\lambda_1)\|$ denotes one half of the chord length.

Using $f_c(x_c,\lambda_1,\lambda_2)$ to denote the object function on the chord, we have

$$f(\vec{r}) = f_c(x_c,\lambda_1,\lambda_2), \tag{8}$$

where $\vec{r}$ and $x_c$ are related through Eq. (7). Because the compact support of the object function is enclosed by the trajectory, the support of the object function on a chord is finite. Without loss of generality, we assume that the object support on the chord is given by $x_c \in [x_{s1},x_{s2}]$. Considering a segment $[x_{c1},x_{c2}]$ on the chord that contains the support $x_c \in [x_{s1},x_{s2}]$, i.e., $[x_{sl},x_{s2}] \subset [x_{c1},x_{c2}]$, one has

$$f_c(x_c,\lambda_1,\lambda_2) = 0 \quad \text{for } x_c \notin [x_{s1},x_{s2}]. \tag{9}$$

From cone-beam data $g(\lambda,\hat{\theta})$, one can compute a backprojection image onto the chord as

$$g_B(x_c,\lambda_1,\lambda_2) = \int_{\lambda_1}^{\lambda_2} \frac{d\lambda}{\|\vec{r} - \vec{r}_0(\lambda)\|}\left[\frac{\partial}{\partial\lambda} g(\lambda,\hat{\theta})\right]_{\hat{\theta}}, \tag{10}$$

where $\vec{r}$ and $x_c$ are related through Eq. (7). Based upon the backprojection image on the chord, the BPF algorithm reconstructs the object function $f_c(x_c,\lambda_1,\lambda_2)$ on the chord as

$$\begin{aligned} f_c(x_c,\lambda_1,\lambda_2) = {} & \frac{1}{2\pi^2}\frac{1}{\sqrt{(x_{c2}-x_c)(x_c-x_{c1})}} \\ & \times \left[\int_{x_{c1}}^{x_{c2}} \frac{dx_c'}{x_c - x_c'}\sqrt{(x_{c2}-x_c')(x_c'-x_{c1})}\right. \\ & \left. \times g_B(x_c',\lambda_1,\lambda_2) + C\right], \end{aligned} \tag{11}$$

where $x_c \in [x_{c1},x_{c2}]$, and the constant $C$ is given by

$$C = 2\pi\int_{x_{c1}}^{x_{c2}} f_c(x_c,\lambda_1,\lambda_2)dx_c = 2\pi g(\lambda_1,\hat{e}_c). \tag{12}$$

### III.B. Chord-based reconstructible volume

For a reverse helical trajectory, we define a one-turn trajectory segment as the portion in which the rotation direction of the source remains unchanged. The chords of a reverse helical trajectory can thus be divided into two classes: chords connecting two points within a one-turn trajectory segment, and chords connecting two points on two different one-turn trajectory segments, which we refer to as one-turn and multiple-turn chords, respectively. For a one-turn chord specified by $\lambda_1$ and $\lambda_2$, $|\lambda_1 - \lambda_2| \le 2\pi$. Therefore, a one-turn chord of a reverse helical trajectory is equivalent to the PI-line segment in a conventional helical trajectory. We display in Figs. 3(a) and 3(b) one-turn and multiple-turn chords for a two-turn reverse helical trajectory.

It has been shown that each point enclosed by the conventional helical trajectory is intersected by at least one chord, and consequently that the volume enclosed can be covered completely by chords.[16] Therefore, the image within the volume enclosed by the conventional helical trajectory can be reconstructed through reconstructing images on chords intersecting with the volume. In a reverse helical trajectory with a

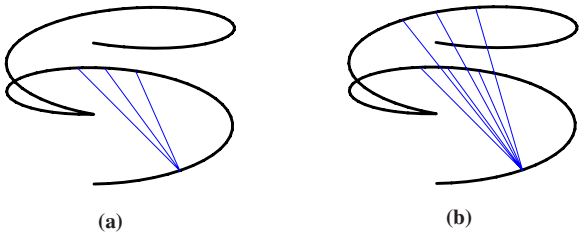

(a) (b)

FIG. 3. Illustration of chords (thin line segments) on a two-turn reverse helical trajectory (thick curve): one-turn chords (a), and multiple-turn chords (b).

finite number of turns, however, as shown in the Appendix, region(s) exist that are not intersected by any chords, and thus image(s) within the region(s) cannot be reconstructed by use of the chord-based algorithms. For a given reverse helical trajectory, one can determine the reconstructible volume by use of the chord-based algorithm through computing the volume covered by the chords. In Fig. 4, we demonstrate the volumes covered by one-turn chords and multiple-turn chords for a two-turn reverse helical trajectory, which are the reconstructible volumes by use of the chord-based algorithms. Specifically, the white regions in Fig. 4 display the reconstructible areas by use of one-turn chords (a) and multiple-turn chords (b) on the sagittal (top row), coronal (middle row), and transverse (bottom row), respectively. Clearly, regions that are not covered by any chords exist for a two-turn reverse helical trajectory; and the use of multiple-turn chords can increase the reconstructible volume.

## IV. FBP ALGORITHM FOR A REVERSE HELICAL TRAJECTORY

In this section, using Pack–Noo's formula, we derive a FBP algorithm for image reconstruction from data acquired with a reversed helical trajectory.

(a) (b)

FIG. 4. Regions (white) covered by one-turn chords (a) and two-turn chords (b) within slices specified by $x=0$ (top row), $y=0$ (middle row), and $z=0$ (bottom row), respectively. Therefore, the white regions represent the reconstructible regions by use of the chord-based algorithms.

### IV.A. Pack–Noo's reconstruction formula

Pack–Noo's formula provides a basis for deriving FBP algorithms for image reconstruction for a general source trajectory.[17,20] For a continuous segment of a trajectory $\vec{r}_0(\lambda)$ that begins and ends at $\lambda^-$ and $\lambda^+$, we divide it into $N$ adjacent, continuous subsegment trajectories of which the $i$th subsegment trajectory begins and ends at $\lambda_i$ and $\lambda_{i+1}$, where $i=1,2,\ldots N$, $\lambda_1=\lambda^-$, and $\lambda_{N+1}=\lambda^+$. Therefore, $[\lambda^-,\lambda^+]=[\lambda_1,\lambda_2]\cup[\lambda_2,\lambda_3]\cup\cdots[\lambda_i,\lambda_{i+1}]\cup\cdots[\lambda_N,\lambda_{N+1}]$. For each of the subsegment trajectories, Pack–Noo's formula provides a reconstruction as

$$\mathcal{K}(\vec{r},\hat{e}_i,\lambda_i,\lambda_{i+1}) = -\frac{1}{2\pi^2}\int_{\lambda_i}^{\lambda_{i+1}} d\lambda \frac{1}{\|\vec{r}-\vec{r}_0(\lambda)\|} g_F(\lambda,\vec{r},\hat{e}_i), \tag{13}$$

where $g_F(\lambda,\vec{r},\hat{e}_i)$ represents the filtered backprojection data, given by

$$g_F(\lambda,\vec{r},\hat{e}_i) = \int_{-\pi}^{\pi} d\gamma \frac{1}{\sin\gamma} \frac{\partial g(\lambda,\hat{\theta}(\lambda,\vec{r},\hat{e}_i,\gamma))}{\partial\lambda}, \tag{14}$$

$$\hat{\theta}(\lambda,\vec{r},\hat{e}_i,\gamma) = \cos\gamma\hat{\alpha}(\lambda,\vec{r}) + \sin\gamma\hat{\beta}(\lambda,\vec{r},\hat{e}_i), \tag{15}$$

$$\hat{\beta}(\lambda,\vec{r},\hat{e}_i) = \frac{\hat{e}_i - (\hat{e}_i\cdot\hat{\alpha}(\lambda,\vec{r}))\hat{\alpha}(\lambda,\vec{r})}{\|\hat{e}_i - (\hat{e}_i\cdot\hat{\alpha}(\lambda,\vec{r}))\hat{\alpha}(\lambda,\vec{r})\|}, \tag{16}$$

and

$$\hat{\alpha}(\lambda,\vec{r}) = \frac{\vec{r}-\vec{r}_0(\lambda)}{\|\vec{r}-\vec{r}_0(\lambda)\|}. \tag{17}$$

The integration over $\gamma$ in Eq. (14) indicates a filtering process over the data derivative, while the filtering direction is determined by a preselected unit vector $\hat{e}_i \in S^2$ for a subsegment trajectory specified by $[\lambda_i,\lambda_{i+1}]$. As discussed below, the specific form of a derived FBP reconstruction algorithm depends critically upon an appropriate selection of $\hat{e}_i \in S^2$.

For a given subsegment trajectory $[\lambda_i,\lambda_{i+1}]$ and a selected unit vector $\hat{e}_i$, the reconstruction term $\mathcal{K}(\vec{r},\hat{e}_i,\lambda_i,\lambda_{i+1})$, as indicated in Eq. (13), can be computed from cone-beam projections and can thus be interpreted as the known data function. Let $(R''f)(\hat{\omega},\vec{r}\cdot\hat{\omega})$ denote the second order derivative of the 3D Radon transform of the object function $f(\vec{r})$. Pack–Noo's formula[17] establishes a relationship between $\mathcal{K}(\vec{r},\hat{e}_i,\lambda_i,\lambda_{i+1})$ and $(R''f)(\hat{\omega},\vec{r}\cdot\hat{\omega})$ as

$$\mathcal{K}(\vec{r},\hat{e}_i,\lambda_i,\lambda_{i+1}) = -\frac{1}{8\pi^2}\int_{S^2} d\hat{\omega}(R''f) \times(\hat{\omega},\vec{r}\cdot\hat{\omega})\sigma(\vec{r},\hat{\omega},\hat{e}_i,\lambda_i,\lambda_{i+1}), \tag{18}$$

where

$$\sigma(\vec{r},\hat{\omega},\hat{e}_i,\lambda_i,\lambda_{i+1}) = \frac{1}{2}\,\mathrm{sgn}(\hat{\omega}\cdot\hat{e}_i)[\mathrm{sgn}(\hat{\omega}\cdot\hat{\alpha}(\lambda_i,\vec{r})) - \mathrm{sgn}(\hat{\omega}\cdot\hat{\alpha}(\lambda_{i+1},\vec{r}))] \tag{19}$$

and "sgn" denotes the signum function. Therefore, for the $N$

continuous subsegment trajectories covering the entire trajectory $\lambda \in [\lambda^-, \lambda^+]$, we have

$$\sum_{i=1}^{N} \mathcal{K}(\vec{r}, \hat{e}_i, \lambda_i, \lambda_{i+1}) = -\frac{1}{8\pi^2} \int_{S^2} d\hat{\omega} (R''f) \times (\hat{\omega}, \vec{r} \cdot \hat{\omega}) \overline{\sigma}(\vec{r}, \hat{\omega}, \lambda^-, \lambda^+), \quad (20)$$

where

$$\overline{\sigma}(\vec{r}, \hat{\omega}, \lambda^-, \lambda^+) = \sum_{i=1}^{N} \sigma(\vec{r}, \hat{\omega}, \hat{e}_i, \lambda_i, \lambda_{i+1}). \quad (21)$$

It can be observed that, if the weighting function

$$\overline{\sigma}(\vec{r}, \hat{\omega}, \lambda^-, \lambda^+) = P = \text{const.}, \quad (22)$$

the right-hand side of Eq. (20) yields exactly $P$ times the inverse 3D radon transform of the object function. Under the condition in Eq. (22), the object function $f(\vec{r})$ is obtained as

$$f(\vec{x}) = \frac{1}{P} \sum_{i=1}^{N} \mathcal{K}(\vec{r}, \hat{e}_i, \lambda_i, \lambda_{i+1}). \quad (23)$$

The result in Eq. (23) is referred to as the FBP reconstruction algorithm, and its derivation, as discussed above, depends upon the appropriate selection of the unit vectors $\{\hat{e}_i\}$ for determining the filtering directions and upon the calculation of $\{\mathcal{K}(\vec{r}, \hat{e}_i, \lambda_i, \lambda_{i+1})\}$.

### IV.B. The FBP algorithm for reverse helical trajectories

Using Pack–Noo's formula, we derive below a FBP algorithm for image reconstruction from cone-beam data acquired with a two-turn reverse helical trajectory. Extension of the derived algorithm to multiple-turn reverse helical trajectories is straightforward and will be briefly described.

For a continuous scanning trajectory, one can define a polygon plane as the plane that intersects the trajectory at more than two points. For each side of a polygon, there exists a continuous subsegment of the source trajectory connecting two ends of the side of the polygon. Based on Pack–Noo's formula, a polygon-based FBP algorithm has been developed for image reconstruction for circular sinusoidal trajectories, including the saddle trajectory.[18] For a circular sinusoidal trajectory, without loss of generality, we consider a polygon of four sides that intersects the trajectory four times. Let unit vectors $\hat{e}_i$ denote the directions of the polygon sides, i.e.,

$$\hat{e}_i = \frac{\vec{r}_0(\lambda_{i+1}) - \vec{r}_0(\lambda_i)}{\|\vec{r}_0(\lambda_{i+1}) - \vec{r}_0(\lambda_i)\|}, \quad (24)$$

where $\lambda_i$ and $\lambda_{i+1}$ denote the starting and ending points of the $i$th subsegment trajectory corresponding to the $i$th side of the polygon, and $i=1,2,3$, and 4. In this case, it has been shown[18,21] that

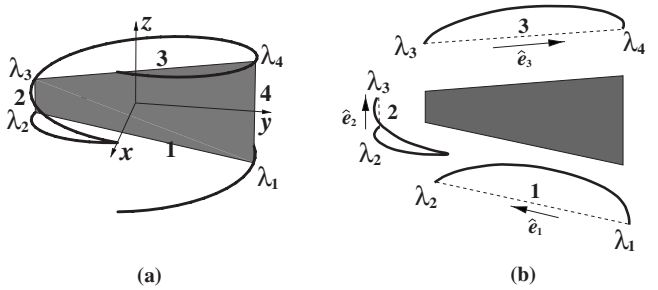


FIG. 5. (a) The four-side polygon (shaded region) formed by four chords each of which connects two points on the two-turn reverse helical trajectory. The polygon plane is chosen to be parallel to $y$-$z$ plane. (b) Continuous subsegment trajectories (thick curves) corresponding to sides $i$ of the four-side polygon (dashed lines), and the directions $\hat{e}_i$ of the chords (i.e., the sides) of the polygon, where $i=1,2$, and 3.

$$\overline{\sigma}(\vec{r}, \hat{\omega}, \lambda^-, \lambda^+) = \sum_{i=1}^{4} \sigma(\vec{r}, \hat{\omega}, \hat{e}_i, \lambda_i, \lambda_{i+1}) = 2, \quad (25)$$

where $\lambda^- = \lambda_1$, $\lambda^+ = \lambda_5$, and $\vec{r}_0(\lambda^+) = \vec{r}_0(\lambda^-)$. Using this result in Eq. (23), one obtains the FBP algorithm for exact image reconstruction within the polygon, which is written as

$$f(\vec{r}) = \frac{1}{2} \sum_{i=1}^{4} \mathcal{K}(\vec{r}, \hat{e}_i, \lambda_i, \lambda_{i+1}). \quad (26)$$

We now extend the FBP algorithm above to reconstruct images for a two-turn reverse helical trajectory depicted in Fig. 5. First of all, it is important to observe, for a given point $\vec{r}$ within and the side direction $\hat{e}_i$ of the polygon, that both $\sigma(\vec{r}, \hat{\omega}, \hat{e}_i, \lambda_i, \lambda_{i+1})$ and $\mathcal{K}(\vec{r}, \hat{e}_i, \lambda_i, \lambda_{i+1})$ depend only upon the starting and ending points $\lambda_i$ and $\lambda_{i+1}$, while being independent of the shape of the continuous subsegment trajectory corresponding to side $i$ of the polygon. Therefore, the results in Eqs. (25) and (26) are directly applicable to image reconstruction within a four-side polygon defined on a general trajectory, under the conditions that (1) $\lambda^- = \lambda_1$, $\lambda^+ = \lambda_5$, and $\vec{r}_0(\lambda^+) = \vec{r}_0(\lambda^-)$ and (2) each side of the polygon has a continuous subsegment trajectory connecting the two ends of the side.

Consider a polygon plane in Fig. 5(a) that is parallel to the $y$-$z$ plane and that intersects the reverse helical trajectory at four distinctive points $\vec{r}_0(\lambda_i)$, where $i=1,\ldots,4$; and $-2\pi \leq \lambda_1 < \lambda_2 \cdots < \lambda_4 \leq 2\pi$. It can be observed in Fig. 5(b) that each of sides 1, 2, and 3 of the polygon has a distinct, continuous subsegment trajectory connecting its two ends. However, side four of the polygon has a distinct, discontinuous subsegment trajectory, which contains the starting and ending points $\lambda_s$ and $\lambda_e$ of the reverse helical trajectory, as displayed in Fig. 6(a). Therefore, Eq. (26) cannot directly be applied to reconstructing an exact image within the polygon for the reverse helical trajectory.

A continuous subsegment trajectory for side four may be formed through including an additional continuous subsegment trajectory that connects the starting point $\lambda_s$ and the ending point $\lambda_e$ of the two-turn reverse helical trajectory. For example, a continuous subsegment trajectory passing $\lambda_s$ and

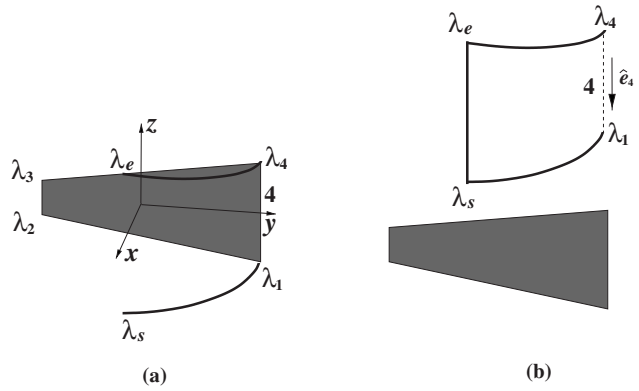


FIG. 6. (a) For side four of the polygon (shade region), the subsegment trajectory containing the starting and ending points $\lambda_s$ and $\lambda_e$ consists of two discontinuous segments (thick curves). (b) A continuous subsegment trajectory passing $\lambda_s$ and $\lambda_e$ can be formed for side four through including, e.g., an additional, straight subsegment trajectory connecting $\lambda_s$ and $\lambda_e$. Again, $\hat{e}_4$ denotes the direction of side four (dashed line) of the polygon.

$\lambda_e$ is formed in Fig. 6(b), which includes an additional, straight subsegment trajectory connecting $\lambda_s$ and $\lambda_e$. However, an additional subsegment trajectory requires an additional scan, thus resulting in additional scanning effort and radiation dose.

It is indeed possible to identify a continuous subsegment trajectory for side four without involving any additional scan to the reverse helical trajectory.[22] As shown in Fig. 7, the union of the three distinct subsegment trajectories corresponding to sides 1, 2, and 3 of the polygon forms a continuous subsegment trajectory for side four of the polygon. As mentioned above, $\mathcal{K}(\vec{r},\hat{e}_4,\lambda_4,\lambda_5)$ is independent of the shape of the continuous subsegment trajectory, while depending only upon $\lambda_4$ and $\lambda_5$, where $\lambda_5$ satisfies $\vec{r}_0(\lambda_5)=\vec{r}_0(\lambda_1)$. Therefore, we can use the union of three distinct subsegment trajectories of sides 1, 2, and 3 to compute $\mathcal{K}(\vec{r},\hat{e}_4,\lambda_4,\lambda_5)$. In fact, from Eq. (5) and Eqs. (13)–(17), it can be seen that $\mathcal{K}(\vec{r},\hat{e}_i,\lambda_i,\lambda_{i+1})$ depends upon $\lambda_i$ and $\lambda_{i+1}$ through $\vec{r}_0(\lambda_i)$ and $\vec{r}_0(\lambda_{i+1})$. Therefore,

$$\mathcal{K}(\vec{r},\hat{e}_4,\lambda_4,\lambda_5)=\mathcal{K}(\vec{r},\hat{e}_4,\lambda_4,\lambda_1), \tag{27}$$

in which we have used $\vec{r}_0(\lambda_5)=\vec{r}_0(\lambda_1)$. Furthermore, using Eq. (13), one can readily show that

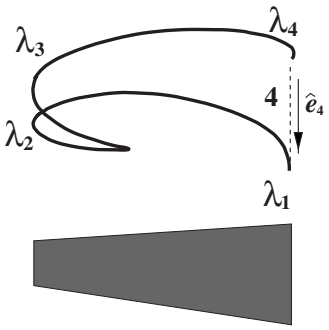


FIG. 7. The portion of a two-turn reverse helical trajectory passing through $\lambda_2$ and $\lambda_3$ forms a continuous subsegment trajectory for side four of the polygon in Fig. 5.

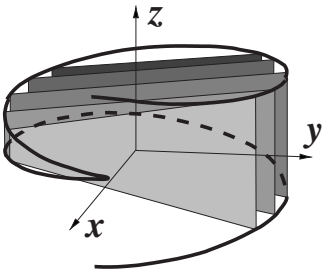


FIG. 8. The volume enclosed by a two-turn reverse helical trajectory can be decomposed into a set of parallel polygons. Without loss of generality, a set of polygons parallel to *y*-*z* plane is shown. A volume image can be obtained through reconstructing images within the polygons by use of the proposed FBP algorithm.

$$\mathcal{K}(\vec{r},\hat{e}_i,\lambda_4,\lambda_1)=-\mathcal{K}(\vec{r},\hat{e}_i,\lambda_1,\lambda_4). \tag{28}$$

Finally, an exact image reconstruction within the polygon for a two-turn reverse helical trajectory can be obtained as

$$f(\vec{r})=\frac{1}{2}\sum_{i=1}^{4}\mathcal{K}(\vec{r},\hat{e}_i,\lambda_i,\lambda_{i+1})=\frac{1}{2}\sum_{i=1}^{3}\mathcal{K}(\vec{r},\hat{e}_i,\lambda_i,\lambda_{i+1})-\frac{1}{2}\mathcal{K}(\vec{r},\hat{e}_4,\lambda_1,\lambda_4). \tag{29}$$

We refer to Eq. (29) as the FBP algorithm for image reconstruction for a reverse helical trajectory. As shown in Fig. 8, the volume enclosed by a reverse helical trajectory can be decomposed into a set of polygons. Therefore, one can achieve a volume-image reconstruction for a reverse helical trajectory through reconstructing images within the set of polygons by use of the FBP algorithm described.

The FBP algorithm above was derived for a two-turn reverse helical trajectory. Similar approach can readily be applied to deriving an FBP algorithm for multiple-turn reverse helical trajectories. Without loss of generality, we use a three-turn reverse helical trajectory to illustrate such an extension. Again, for the given reverse helical trajectory, we first select a four-side polygon whose four corners reside on the trajectory, as shown in Fig. 9. In the case of a multiple-turn reverse helical trajectory, different polygons can be devised. In Figs. 9(a) and 9(b), two different four-side polygons are displayed. In these cases, it can be readily shown that,

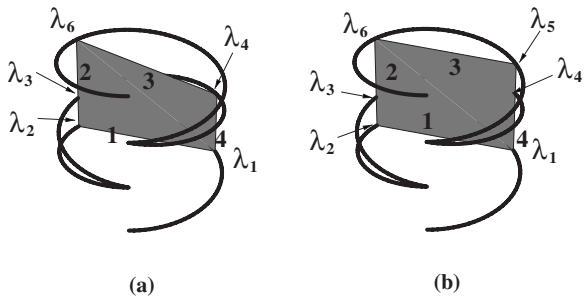


FIG. 9. (a) A polygon with four corners intersecting the three-turn reverse helical trajectory at $\lambda_1$, $\lambda_2$, $\lambda_4$, and $\lambda_6$. (b) A polygon with four corners intersecting the three-turn reverse helical trajectory at $\lambda_1$, $\lambda_2$, $\lambda_5$, and $\lambda_6$.

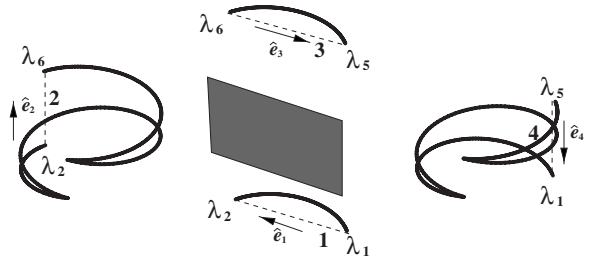


FIG. 10. The continuous subsegment trajectories corresponding to each side of the polygon in Fig. 9(b).

when unit vectors $\{\hat{e}_i\}$ are selected along each of the sides of the polygon, the result in Eq. (25) remains unchanged. Furthermore, a continuous subsegment trajectory can be identified for each side of the polygon. In Fig. 10, we display the continuous subsegment trajectories for each side of the polygon in Fig. 9(b). From these continuous subsegment trajectories, one can compute $\mathcal{K}(\vec{r},\hat{e}_i,\lambda_i,\lambda_{i+1})$ and use them in Eq. (29) to obtain the image within the polygon. Finally, one can obtain a volume image by reconstructing 2D images within a set of polygons in the volume enclosed by the reverse helical trajectories, as displayed in Fig. 11.

## V. NUMERICAL RESULTS

We have performed computer simulation studies to validate that the proposed FBP algorithm can reconstruct images within the volume enclosed by a reverse helical trajectory, including the chordless regions that cannot be reconstructed by use of the chord-based algorithm. A low contrast 3D Shepp–Logan phantom was used that has an ellipsoid support with axes of 13.8, 18.0, and 18.4 cm along the *x*, *y*, and *z* axis, respectively. Additionally, a high contrast shoulder phantom was also used that has an ellipsoid support with axes of 16.0, 8.0, and 8.0 cm along the *x*, *y*, and *z* axis, respectively. The shoulder phantom has been designed specifically to supply *z*-slice images that look like FORBILD thorax phantom and also to prevent data truncation for this study.[23] The details of the shoulder phantom are described in Table I. In the phantom, different types of objects are included: cut ellipsoid (CE) that has cuts along long axis, ellipsoid (E), cone (CN), and cylinder (CL). Parameters represent half lengths of long axis and two other short axes for CE and E; top radius, bottom radius, and height for CN; and radius and height for CL. Polar ($\theta$) and azimuthal ($\phi$) angles are given in degrees. All the lengths are in relative units, and the phantom has been resized in the numerical study. The reverse helical trajectories have radii of $R=60$ cm and the distances of $D=75$ cm from the sources to detectors. The number of projections per turn is 800. We used helical pitch of $h=40$ cm in the simulation study for the proposed FBP algorithm. For the purpose of clearly demonstrating the chordless region in the reconstruction, we used a helical

TABLE I. Shoulder phantom description.

| Type | Center | Parameters | Cut-length | Angles ($\theta,\phi$) | Density |
|---|---|---|---|---|---|
| CE | 0,0,0 | 80,40,40 | −70,70 | 0,0 | 1.5 |
| CE | −80,0,0 | 22,22,22 | −22,10 | 0,0 | 1.5 |
| CE | 80,0,0 | 22,22,22 | −10,22 | 0,0 | 1.5 |
| E | −88,0,0 | 10,10,10 | | 0,0 | 2.3 |
| E | −88,0,0 | 8,8,8 | | 0,0 | 1.5 |
| E | 88,0,0 | 10,10,10 | | 0,0 | 2.3 |
| E | 88,0,0 | 8,8,8 | | 0,0 | 1.5 |
| E | −65,0,0 | 10,10,10 | | 0,0 | 2.3 |
| E | −65,0,0 | 8,8,8 | | 0,0 | 1.5 |
| E | 65,0,0 | 10,10,10 | | 0,0 | 2.3 |
| E | 65,0,0 | 8,8,8 | | 0,0 | 1.5 |
| E | 0,20,0 | 5,5,5 | | 0,0 | 2.3 |
| CE | 0,20,0 | 6.5,6.5,6.5 | −5.5,6.5 | 0,−90 | 3.0 |
| CN | 0,27.5,0 | 3.5,15,4 | | 0,0 | 3.0 |
| CL | 0,33,0 | 1.5,7 | | 90,90 | 3.0 |
| E | −40,20,0 | 23,3,3 | | 0,20 | 2.3 |
| E | −40,20,0 | 18,2,2 | | 0,20 | 1.5 |
| E | 40,20,0 | 23,3,3 | | 0,−20 | 2.3 |
| E | 40,20,0 | 18,2,2 | | 0,−20 | 1.5 |
| CL | 0,−36,0 | 2,9 | | 90,0 | 2.3 |
| CL | 0,−36,0 | 1,7 | | 90,0 | 1.5 |
| CE | 12,−35,0 | 13,2,2 | −1,13 | 0,20 | 2.3 |
| CE | 12,−35,0 | 10,1,1 | 0,10 | 0,20 | 1.5 |
| CE | −12,−35,0 | 13,2,2 | −13,1 | 0,−20 | 2.3 |
| CE | −12,−35,0 | 10,1,1 | −10,0 | 0,−20 | 1.5 |
| E | −20,5,0 | 4,5,5 | | 0,0 | 2.0 |
| E | −10,−15,0 | 13,15,10 | | 0,−30 | 2.0 |
| E | 20,5,0 | 12,10,10 | | 0,30 | 2.0 |

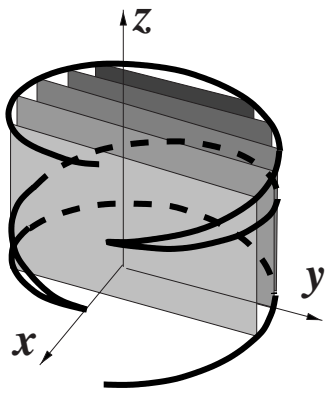


FIG. 11. The volume enclosed by a three-turn reverse helical trajectory can be decomposed into a set of parallel polygons. A set of polygons parallel to *y*-*z* plane is shown here. A volume image can be obtained through reconstructing images within the polygons.

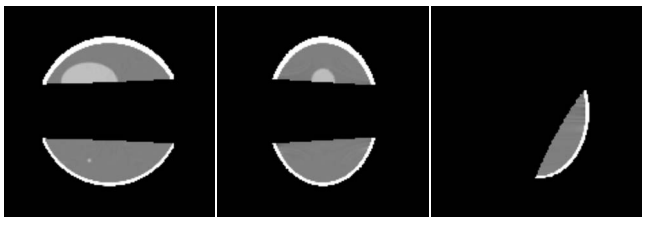


FIG. 12. Images of the Shepp–Logan phantom within slices at (a) $x=0$ cm, (b) $y=0$ cm, and (c) $z=-2.5$ cm reconstructed from noiseless data by use of the chord-based algorithm on one-turn chords. Display window is [1.0,1.04].


FIG. 13. Images of the Shepp–Logan phantom within slices at (a) $x=0$ cm, (b) $y=0$ cm, and (c) $z=-2.5$ cm reconstructed from noiseless data by use of the chord-based algorithm on both one-turn and two-turn chords. Display window is [1.0,1.04].

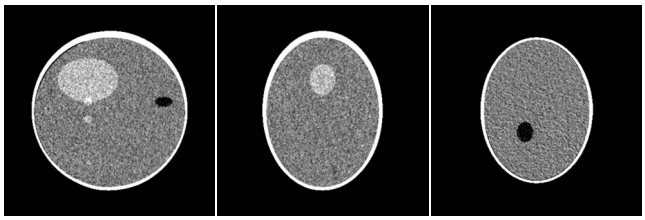


FIG. 15. Images of the Shepp–Logan phantom within slices at (a) $x=0$ cm, (b) $y=0$ cm, and (c) $z=-2.5$ cm reconstructed from the noisy data by use of the proposed FBP algorithm. Display window is [1.01,1.03].

pitch of $h=15$ cm in the simulation study involving the chord-based BPF algorithm. When $h=40$ cm is used for the chord-based BPF algorithm study, the phantom would be barely reconstructed that the difference between the images, reconstructed by use of only one-turn chords and two-turn chords as well, is small. The detector panel considered here has an effective square area that consists of $400\times400$ pixels each of which has a size of $0.78\times0.78$ mm$^2$. Image reconstruction volume consists of $400\times400\times400$ voxels each of which has a size of $0.61\times0.61\times0.61$ mm$^3$. Similar discretization rules to those in Ref. 21 have been used in the implementation of the algorithm, which are summarized in the Appendix B.

In Figs. 12 and 13, we display images of the Shepp–Logan phantom within slices at (a) $x=0$ cm, (b) $y=0$ cm, and (c) $z=-2.5$ cm reconstructed on one-turn and multiple-turn chords by using the chord-based BPF algorithm. Clearly, the BPF algorithm can accurately reconstruct images within the regions covered the chords. Comparison of the reconstructive regions in Figs. 12 and 13 indicates that the use of multiple-turn chords leads to a larger reconstructible region than that only from the one-turn chords. However, it can also be observed in both cases that the BPF algorithm cannot yield images within the chordless regions (e.g., the dark regions between the two reconstructible regions).

In Fig. 14, we show images of the Shepp–Logan phantom within slices at (a) $x=0$ cm, (b) $y=0$ cm, and (c) $z=-2.5$ cm reconstructed by using the proposed FBP algorithm. The results indicate that the proposed algorithm can reconstruct an image within the volume enclosed by a reverse helical trajectory. In an attempt to demonstrate quantitatively the reconstruction accuracy, we display in Fig. 14(d) the profile along a vertical line, specified by $x=0$ cm and $y=-2.5$ cm, passing through the Shepp–Logan phantom, as indicated in Fig. 14(a). For comparison, we also plot the corresponding true profile as dotted curve in Fig. 14(d). The profile results suggest that the proposed FBP algorithm can accurately reconstruct an image within the entire volume enclosed by the reverse helical trajectory. We have also performed a preliminary reconstruction from noisy data by use of the proposed FBP algorithm. We included Gaussian noise in the projection data with the noise level of 0.25%. From the noisy data, we reconstructed images by use of the proposed FBP algorithm. In Fig. 15, we display the reconstructed noisy images within slices at (a) $x=0$ cm, (b) $y=0$ cm, and (c) $z=-2.5$ cm.

In Fig. 16, we show images of the shoulder phantom within slices at (a) $x=0$ cm, (b) $y=0$ cm, and (c) $z=0$ cm reconstructed by using the proposed FBP algorithm. We also display in Fig. 16(d) the profile along a horizontal line, specified by $y=0.5$ cm and $z=0$ cm, passing through the phantom, as indicated in Fig. 16(c). Corresponding true profile is represented by a dotted curve in Fig. 16(d). These results indicate the proposed algorithm can reconstruct high contrast variations accurately as well although some image artifacts due to discretization errors are observable such as streaks in Fig. 16(c). We included Gaussian noise in the projection data with the noise level of 1.0%. From the noisy data, we reconstructed images by use of the proposed FBP algorithm. In Fig. 17, we display the reconstructed noisy images within slices at (a) $x=0$ cm, (b) $y=0$ cm, and (c) $z=0$ cm.

## VI. DISCUSSION

In the work, we have proposed reverse helical trajectories for acquiring cone-beam data, and have investigated and de-

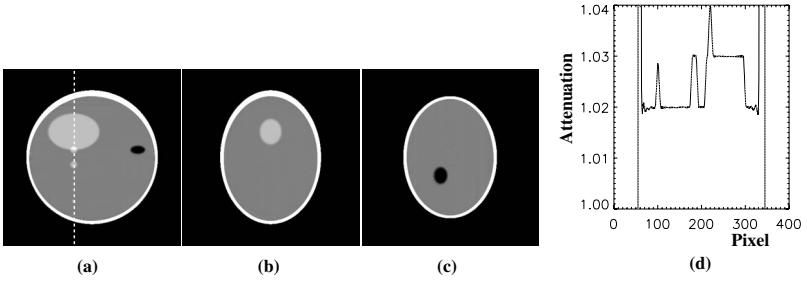


FIG. 14. Images of the Shepp–Logan phantom within slices at (a) $x=0$ cm, (b) $y=0$ cm, and (c) $z=-2.5$ cm reconstructed from noiseless data by use of the proposed FBP algorithm. Display window is [1.0,1.04]. (d) Profile on the vertical line specified by $x=0$ cm and $y=-2.5$ cm, which is also indicated in (a). The reconstructed and true profiles are displayed as solid and dotted curves, respectively.

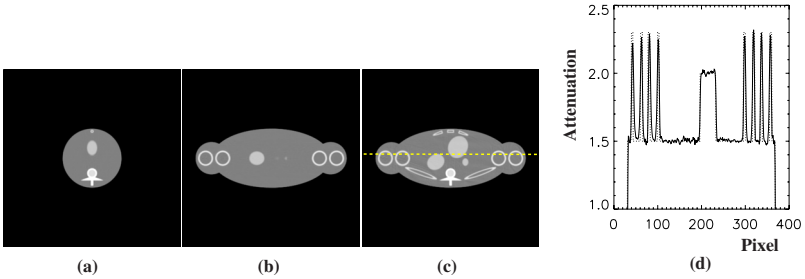


FIG. 16. Images of the shoulder phantom within slices at (a) $x=0$ cm, (b) $y=0$ cm, and (c) $z=0$ cm reconstructed from noiseless data by use of the proposed FBP algorithm. Display window is [1.0,2.5]. (d) Profile on the horizontal line specified by $y=0.5$ cm and $z=0$ cm, which is also indicated in (c). The reconstructed and true profiles are displayed as solid and dotted curves, respectively.

veloped algorithms for image reconstruction from such cone-beam data. The proposed reverse helical trajectories and reconstruction algorithms may find use in IGRT and other applications. Recently, chord-based algorithms such as the BPF algorithm have been developed for image reconstruction from data acquired with general trajectories, provided that the trajectories have chords covering the object. However, reverse helical trajectories are unique in that, although they satisfy Tuy's sufficient data condition for nontruncated object, certain parts of the volume enclosed by them are not covered by chords. Consequently, the chord-based algorithms cannot reconstruct images within the chordless regions of reverse helical trajectories. For a given reverse helical trajectory, we have investigated its chordless regions; and we then conducted image reconstruction by use of the chord-based BPF algorithm to demonstrate the nonreconstructible, chordless regions.

As mentioned above, however, the volume enclosed by a reverse helical trajectory satisfies Tuy's condition, suggesting that exact image of an object within the reverse helix volume including the chordless regions can be reconstructed. We have proposed a FBP algorithm based on Pack–Noo's formula to reconstruct the images within the volume enclosed by a reverse helical trajectory, thus eliminating the chordless region that is nonreconstructible by use of the chord-based algorithms. Numerical studies were also conducted to validate the proposed FBP algorithm. Results of the numerical studies confirm that, unlike the chord-based algorithm, the proposed FBP algorithm can reconstruct an accurate image for the entire reverse helix volume. Since the proposed algorithm is of FBP type, it is in general computationally efficient. However, data filtering has to be performed at least twice for each projection, which may increase the amount of computation compared to a conventional FBP algorithm.

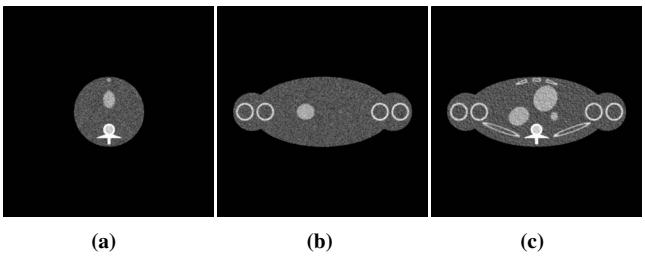


FIG. 17. Images of the shoulder phantom within slices at (a) $x=0$ cm, (b) $y=0$ cm, and (c) $z=0$ cm reconstructed from the noisy data by use of the proposed FBP algorithm. Display window is [1.0,2.5].

Interestingly, the developed FBP algorithm allows certain transverse data truncation. This is because the data filtering is determined only by the directions of the polygon sides within which the image is to be reconstructed. When the polygons covering the reverse helix volume are selected to be, e.g., parallel to the $y$-$z$ plane, as we did here, data truncation along the $x$ axis outside the volume covered by the polygons does not affect the image-reconstruction accuracy within these polygons. However, the proposed FBP algorithm generally allows no truncation longitudinally and is thus incapable of dealing with a long object problem. For a reverse helical trajectory with a long object problem, we are developing a combined image-reconstruction method in which the chord-based algorithm is used for addressing the long object problem, and the proposed FBP algorithm is used for dealing with image reconstruction within the chordless regions. The research of this combined method is beyond the scope of the current work and will be reported elsewhere in the future. We have also discussed the extension of the proposed FBP algorithm to reconstruct images for multiple-turn reverse helical trajectories. In fact, it should be pointed out that the proposed FBP algorithm can readily be generalized to address the problems of image reconstruction for reverse helical trajectories with tilted axis, or variable pitches, or additional scanning trajectory segments.

## ACKNOWLEDGMENTS

S.C. is supported in part by DOD Predoctoral training Grant No. PC061210, and D.X. is supported in part by DOD Predoctoral training Grant No. BC051553. This work was also supported in part by National Institutes of Health Grant Nos. EB00225 and CA120540. Its contents are solely the responsibility of the authors and do not necessarily represent the official views of the National Institutes of Health. The authors would like to thank Dr. Yu Zou for his help on shoulder phantom.

## APPENDIX A: ANALYSIS OF THE CHORDLESS REGIONS IN A REVERSE HELICAL TRAJECTORY

It is shown here that there exist chordless regions in the volume enclosed by a two-turn reverse helical trajectory. For simplifying the discussion, we consider intersecting points along $z$ axis, which is the rotation axis, with all the possible chords, and we show that there exists a region between intersecting regions on $z$ axis. A chord passing through $z$ axis defines a unique plane containing the chord and $z$ axis. For a

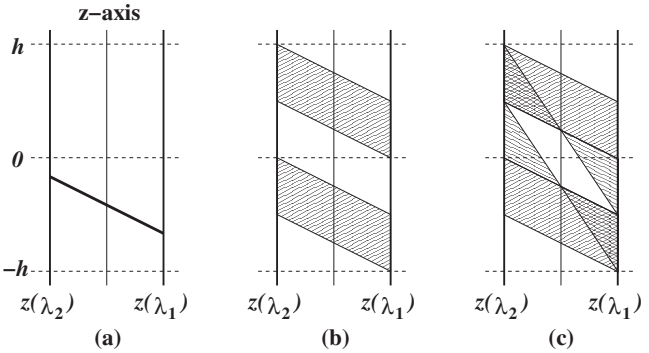


FIG. 18. Diagrams demonstrating the chordless region along $z$ axis for a two-turn reverse helical trajectory. (a) An exemplary chord plotted on the plane defined by the chord and $z$ axis. (b) Collection of all one-turn chords. (c) Collection of all chords including multiple-turn chords.

given chord passing through $z$ axis, we label the angular parameter of the lower end by $\lambda_1$ and that of the upper end by $\lambda_2$. A chord, for example, is presented on the defined plane in Fig. 18. Using circular symmetry, we can establish the functional relationship, as summarized in Table II, between $z(\lambda_1)$ and $z(\lambda_2)$ for one-turn chords and also for multiple-turn chords, where $z(\lambda)$ indicates the $z$ coordinate of a source point on the reverse helical trajectory at $\lambda$. The $z$-coordinate, $z_0(\lambda_1,\lambda_2)$, of the intersecting point of a chord withz axis is given by

$$z_0(\lambda_1,\lambda_2)=\frac{1}{2}[z(\lambda_1)+z(\lambda_2)], \tag{A1}$$

which is in the shaded regions in Figs. 18(a) and 18(b) for one-turn and multiple-turn chords. The chordless (white) region can be observed between the intersecting (shaded) regions.

## APPENDIX B: IMPLEMENTATION OF THE PROPOSED FBP ALGORITHM

For discussion of algorithm implementation, we introduce a rotation-coordinate system $\{u,v,w\}$ in which its origin is on the source $\vec{r}_0(\lambda)$, and its $u$-$w$ plane and $v$ axis are parallel to the $x$-$y$ plane and to the $z$ axis, respectively, of the fixed-coordinate system $\{x,y,z\}$. The unit vectors of the rotation-coordinate system at a scanning angle $\lambda$ can be expressed in the fixed-coordinate system as

$$\hat{e}_u(\lambda)=(-\sin\lambda,\cos\lambda,0)$$

$$\hat{e}_v(\lambda)=(0,0,1)$$

$$\hat{e}_w(\lambda)=(\cos\lambda,\sin\lambda,0). \tag{B1}$$

Let the flat-panel detector be placed within a plane at $w=-D$ that is parallel to the $u$-$v$ plane. We introduce a 2D-detector-coordinate system $\{u_d,v_d\}$ on the plane in which the $u_d$ and $v_d$ axes are parallel to the $u$ and $v$ axes, respectively, and its origin is at the projection, along $\hat{e}_w$, on the detector plane, of the source point $\vec{r}_0(\lambda)$. For a point $\vec{x}_d$ on the detector plane, the relationship between its fixed coordinates $(x_d,y_d,z_d)$ and 2D-detector coordinates $(u_d,v_d)$ can be obtained as

$$x_d=-u_d\sin\lambda+(-D+R)\cos\lambda$$

$$y_d=u_d\cos\lambda+(-D+R)\sin\lambda$$

$$z_d=v_d+\frac{h}{2\pi}\lambda. \tag{B2}$$

Now the three steps of the algorithm can be summarized as follows.

*Data derivative*: We compute

$$\frac{\partial g(\lambda,\hat{\theta})}{\partial\lambda}=\frac{\partial g(\lambda,u_d,v_d)}{\partial\lambda}=\left(\frac{\partial}{\partial\lambda}+\frac{D^2+u_d^2}{D}\frac{\partial}{\partial u_d}+\frac{u_dv_d}{D}\frac{\partial}{\partial v_d}\right)g(\lambda,u_d,v_d). \tag{B3}$$

Three points differentiation method has been used for computing derivatives.

*Hilbert transform*: For given filtering direction $\hat{e}$, we compute 1D Hilbert transform along the projection of $\hat{e}$ at image point $\vec{r}$ onto the detector as

$$g_F(\lambda,\vec{r},\hat{e})=g_F(\lambda,u_d,v_d,\hat{e})=\int_{u_l}^{u_u}du_d'\frac{A}{A'}h_H(u_d-u_d')\frac{\partial g(\lambda,u_d',v_d')}{\partial\lambda}, \tag{B4}$$

where $h_H(u)$ is the kernel of Hilbert transform, $A=\sqrt{D^2+u_d^2+v_d^2}$, and $A'=\sqrt{D^2+u_d'^2+v_d'^2}$. Upper and lower integration boundaries can be either $(-\infty,\infty)$ or $(\infty,-\infty)$ depending on the relative position $\vec{r}_0(\lambda)$ with respect to the reconstruction point $\vec{r}$. Rebinning and back-rebinning method similar to that used in Ref. 21 has been used for integration.

*Backprojection*: We compute

TABLE II. Relationship between the $z$ coordinates of chords passing through $z$ axis for a two-turn reverse helical trajectory.

| | $\lambda_1$ | $-2\pi\le\lambda_1\le-\pi$ | $-\pi<\lambda_1<0$ | $0\le\lambda_1\le\pi$ | $\pi<\lambda_1\le2\pi$ |
|---|---|---|---|---|---|
| | $z(\lambda_1)$ | $h/2\pi(\lambda_1)$ | $h/2\pi(\lambda_1)$ | $h/2\pi(\lambda_1)$ | $h/2\pi(\lambda_1)$ |
| One-turn chords | $z(\lambda_1)$ | $h/2\pi(\lambda_1+\pi)$ | None | $h/2\pi(\lambda_1+\pi)$ | None |
| Multiple-turn chords | $z(\lambda_2)$ | $h/2\pi(-\lambda_1-\pi)$ | $h/2\pi(-\lambda_1+\pi)$ | None | None |

$$\mathcal{K}(\vec{r},\hat{e}_i,\lambda_i,\lambda_{i+1}) = -\frac{1}{2\pi^2}\int_{\lambda_i}^{\lambda_{i+1}} d\lambda \frac{1}{\|\vec{r}-\vec{r}_0(\lambda)\|} g_F(\lambda,\vec{r},\hat{e}_i). \tag{B5}$$

Bilinear interpolation has been used for computing the backprojection.

[a]Author to whom correspondence should be addressed. Electronic mail: xpan@uchicago.edu

[1]D. A. Jaffray and J. H. Siewerdsen, "Cone-beam computed tomography with a flat-panel imager: Initial performance characterization," Med. Phys. **27**, 1311–1323 (2000).
[2]J. H. Siewerdsen and D. A. Jaffray, "Optimization of x-ray imaging geometry (with specific application to flat-panel cone-beam computed tomography)," Med. Phys. **27**, 1903–1914 (2000).
[3]B. A. Groh, J. H. Siewerdsen, D. G. Drake, J. W. Wong, and D. A. Jaffray, "A performance comparison of flat-panel imager-based MV and kV cone-beam CT," Med. Phys. **29**, 967–975 (2002).
[4]L. A. Feldkamp, L. C. Davis, and J. W. Kress, "Practical cone-beam algorithm," J. Opt. Soc. Am. **A1**, 612–619 (1984).
[5]S. Mori, M. Endo, S. Komatsu, S. Kandatsu, T. Yashiro, and M. Baba, "A combination-weighted Feldkamp-based reconstruction algorithm for cone-beam CT," Phys. Med. Biol. **51**, 3953–3965 (2006).
[6]S. Valton, F. Peyrin, and D. Sappey-Marinier, "Analysis of cone-beam artifacts in off-centered circular CT for four reconstruction methods," Int. J. Biomed. Imaging **2006**, 1–8 (2006).
[7]S. Yoo and F. Yin, "TU-FF-A2-01: Feasibility of cone-beam CT based treatment planning," Med. Phys. **33**, 2219 (2006).
[8]A. Katsevich, "Theoretically exact FBP-type inversion algorithm for spiral CT," SIAM J. Appl. Math. **62**, 2012–2026 (2002).
[9]F. Noo, J. Pack, and D. Heuscher, "Exact helical reconstruction using native cone-beam geometries," Phys. Med. Biol. **48**, 3787–3818 (2003).
[10]Y. Zou and X. Pan, "Exact image reconstruction on PI-line from minimum data in helical cone-beam CT," Phys. Med. Biol. **49**, 941–959 (2004).
[11]Y. Ye and G. Wang, "Filtered backprojection formula for exact image reconstruction from cone-beam data along a general scanning curve," Med. Phys. **32**, 654–665 (2005).
[12]J. D. Pack, F. Noo, and R. Clackdoyle, "Cone-beam reconstruction using the backprojection of locally filtered projections," IEEE Trans. Med. Imaging **24**, 2317–2336 (2005).
[13]Y. Zou, X. Pan, and E. Y. Sidky, "Theory and algorithms for image reconstruction on chords and within regions of interest," J. Opt. Soc. Am. **22**, 2372–2384 (2005).
[14]A. Katsevich, "Image reconstruction for the circle-arc trajectory," Phys. Med. Biol. **50**, 2249–2265 (2005).
[15]T. Zhuang and G. Chen, "New families of exact fan-beam and cone-beam image reconstruction formulae via filtering the backprojection image of differentiated projection data along singly measured lines," Inverse Probl. **22**, 991–1006 (2006).
[16]P. E. Danielsson, P. Edholm, and M. Seger, "Towards exact 3D-reconstruction for helical cone-beam scanning of long objects. A new detector arrangement and a new completeness condition," in *Proceedings of the 1997 International Meeting on Fully Three-Dimensional Image Reconstruction in Radiology and Nuclear Medicine*, edited by D. W. Townsend and P. E. Kinahan, Pittsburgh, 1997.
[17]J. D. Pack and F. Noo, "Cone-beam reconstruction using 1D filtering along the projection of M-lines," Inverse Probl. **21**, 1105–1120 (2005).
[18]H. Yang, M. Li, K. Koizumi, and H. Kudo, "Application of Pack and Noo's cone-beam inversion formula to a wide class of trajectories," in *IEEE Medical Imaging Conference Record*, San Diego, CA, 2006, pp. M14–450.
[19]E. Y. Sidky, Y. Zou, and X. Pan, "Minimum data image reconstruction algorithms with shift-invariant filtering for helical, cone-beam CT," Phys. Med. Biol. **50**, 1643–1657 (2005).
[20]J. D. Pack and F. Noo, "Cone-beam reconstruction outside R-lines using the backprojection of 1-D filtered data," in *Proceedings of the 2005 International Meeting on Fully Three-Dimensional Image Reconstruction in Radiology and Nuclear Medicine*, Salt Lake City, UT, pp. 287–290 (2005).
[21]H. Yang, M. Li, K. Koizumi, and H. Kudo, "Exact cone beam reconstruction for a saddle trajectory," Phys. Med. Biol. **51**, 1157–1172 (2006).
[22]D. Xia, S. Cho, and X. Pan, "Image reconstruction for cone-beam CT with reduced-scan circular sinusoidal trajectories," IEEE Trans. Med. Imaging (submitted).
[23]http://www.imp.uni erlangen.de/phantoms/thorax/thorax.htm

# A BPF-FBP tandem algorithm for image reconstruction in reverse helical cone-beam CT

Seungryong Cho
*Department of Radiology and Department of Radiation and Cellular Oncology, University of Chicago, Chicago, Illinois 60637*

Dan Xia
*Department of Radiology, University of Chicago, Chicago, Illinois 60637*

Charles A. Pellizzari
*Department of Radiation and Cellular Oncology, University of Chicago, Chicago, Illinois 60637*

Xiaochuan Pan[a)]
*Department of Radiology and Department of Radiation and Cellular Oncology, University of Chicago, Chicago, Illinois 60637*

(Received 13 July 2009; revised 16 September 2009; accepted for publication 22 October 2009; published 4 December 2009)

**Purpose:** Reverse helical cone-beam computed tomography (CBCT) is a scanning configuration for potential applications in image-guided radiation therapy in which an accurate anatomic image of the patient is needed for image-guidance procedures. The authors previously developed an algorithm for image reconstruction from nontruncated data of an object that is completely within the reverse helix. The purpose of this work is to develop an image reconstruction approach for reverse helical CBCT of a long object that extends out of the reverse helix and therefore constitutes data truncation.
**Methods:** The proposed approach comprises of two reconstruction steps. In the first step, a chord-based backprojection-filtration (BPF) algorithm reconstructs a volumetric image of an object from the original cone-beam data. Because there exists a chordless region in the middle of the reverse helix, the image obtained in the first step contains an unreconstructed central-gap region. In the second step, the gap region is reconstructed by use of a Pack–Noo-formula-based filteredback-projection (FBP) algorithm from the modified cone-beam data obtained by subtracting from the original cone-beam data the reprojection of the image reconstructed in the first step.
**Results:** The authors have performed numerical studies to validate the proposed approach in image reconstruction from reverse helical cone-beam data. The results confirm that the proposed approach can reconstruct accurate images of a long object without suffering from data-truncation artifacts or cone-angle artifacts.
**Conclusions:** They developed and validated a BPF-FBP tandem algorithm to reconstruct images of a long object from reverse helical cone-beam data. The chord-based BPF algorithm was utilized for converting the long-object problem into a short-object problem. The proposed approach is applicable to other scanning configurations such as reduced circular sinusoidal trajectories. © *2010 American Association of Physicists in Medicine*. [DOI: 10.1118/1.3263618]

Key words: cone-beam CT, image reconstruction, reverse helical, BPF, FBP

## I. INTRODUCTION

Cone-beam computed tomography (CBCT) is one of the most popular modalities for image-guidance procedures such as patient setup and target localization in radiation therapy.[1–3] Current technologies employed in clinical CBCT systems are based on a circular scanning geometry for data acquisition, and on algorithms such as the Feldkamp–Davis–Kress (FDK) algorithm[4] for image reconstruction. Although images produced by these algorithms from circular cone-beam data are often acceptable for practical tasks, it is of interest to work toward enhanced image quality, thus leading to increased utility of CBCT in a variety of image-guided radiation therapy (IGRT) applications. Accurate images are particularly important in on-line adaptive radiation therapy, where CBCT images may be used for treatment replanning.[5,6]

Although helical CBCT is well known to provide sufficient data for exact image reconstruction, a conventional helical CBCT with multiple turns would be difficult to achieve on an existing linear accelerator (LINAC) system because the gantry of a LINAC treatment system cannot rotate more than one turn in a single direction. Reverse helical CBCT, on the other hand, can be realized by reversing the gantry rotation after each turn while continuously translating the patient couch. Therefore, we have previously investigated reverse helical CBCT for potential use in IGRT and explored image-reconstruction algorithms for reverse helical CBCT.[7]

In the past decade, significant advances have been made in algorithm development for accurate image reconstruction in helical CBCT, including filtered-backprojection (FBP) algorithms[8,9] and chord-based algorithms.[10–12] These algorithms have also been extended to image reconstruction from general source trajectories.[13,14] In a chord-based algorithm, the image is decomposed into chords each of which is a line segment connecting two points on a continuous source trajectory. The object image is obtained by reconstructing images on the chords intersecting the object. The chord-based algorithms can be applied to general source trajectories. One of the chord-based algorithms, which is referred to as the backprojection filtration (BPF) algorithm, can reconstruct accurate images within regions of interest (ROIs) from data containing truncations.[13] However, because of the dependence of chord-based algorithms on the existence of chords, they cannot reconstruct images in chordless regions even though sufficient cone-beam data are provided.[12] For a reverse helical trajectory, it has been shown that there exists a chordless gap, which cannot be reconstructed by use of the chord-based BPF algorithm.[7]

The Pack–Noo formula relates a 3D inverse Radon transform to a FBP of the conebeam data and can be used for image reconstruction from data that satisfy Tuy's data sufficiency condition for exact image reconstruction in CBCT.[12,15] Based on the Pack–Noo formula, a useful approach was developed for image reconstruction in CBCT with an umbrella trajectory[16] and with general, closed trajectories.[17] In that approach, the volumetric image is decomposed into polygon planes, which are defined by the intersection of planes with the source trajectory, and the images within the polygon planes are reconstructed through backprojecting the filtered data onto the polygons. The direction of a polygon side, which is by definition a chord, is used as the filtering direction in the reconstruction. We have applied this approach to image reconstruction in CBCT with general, open source trajectories.[7,18] Because the Pack–Noo-formula-based algorithm is not dependent on the existence of chords, it can reconstruct an image within the chordless region where chord-based algorithms cannot. However, this algorithm can accurately reconstruct images only from nontruncated data of a short object that is completely enclosed by the polygons for a reverse helical trajectory.

In practice, the imaged object, e.g., a patient, is usually too long to be confined within the trajectory in a reverse helical CBCT, thus constituting the data truncation problem of a long object. In an attempt to address this long object problem in the reverse helical scan, we propose a BPF-FBP tandem algorithm that utilizes advantages of each of the algorithms for image reconstruction in reverse helical CBCT. The key of the proposed tandem algorithm lies in the observation that the chord-based BPF algorithm can be utilized for converting a long-object problem into a short-object problem confined to the chordless middle gap, which can then be reconstructed by the use of the Pack–Noo-formula-based algorithm. Specifically, the chord-based BPF algorithm reconstructs parts of the object volume from the original cone-beam data first, and the Pack–Noo-formula-based FBP algorithm reconstructs the middle gap region from the residual cone-beam data obtained by subtracting the reprojection of the BPF-reconstructed image from the original data. We perform numerical studies in which the NCAT phantom[19] is used to validate and demonstrate the proposed approach.

## II. BPF-FBP TANDEM ALGORITHM

The proposed algorithm is composed of two reconstruction steps in sequence. The first reconstruction is conducted by the use of the chord-based BPF algorithm. The chord-based BPF algorithm can deal with the longitudinal data truncation that occurs in a patient scan, and an exact volumetric image can be obtained, although the image contains a middle gap where no chords are available. The reconstructed volume image is then reprojected to produce cone-beam data corresponding to the scanning configuration that was used for acquiring the original cone-beam data. Subtracting the reprojected cone-beam data from the original cone-beam data yields the cone-beam data for the parts that are not reconstructible by the chord-based BPF algorithm. The resulting cone-beam projection contains three regions: Top, middle, and bottom parts. The top and bottom parts of each cone-beam projection, which correspond to inherently unreconstructible regions of the object at the ends of the trajectory, are removed, and the middle portion is used for the second step reconstruction with the Pack–Noo-formula-based FBP algorithm. After the second step reconstruction, the final image is obtained by combining the two reconstructed images. The algorithm is illustrated in this section after introducing the reverse helical trajectory.

### II.A. Reverse helical trajectory

A reverse helical trajectory $\vec{r}_0(\lambda)$ can be expressed as

$$\vec{r}_0(\lambda)=\left(R\cos((-1)^n\lambda),R\sin((-1)^n\lambda),\frac{h}{2\pi}\lambda\right),$$

$$\lambda\in[\lambda_s,\lambda_e], \tag{1}$$

where $R$ denotes the distance from the source to the rotation axis, $h$ is the helical pitch, and $\lambda_s$ and $\lambda_e$ are the starting and ending angles of the trajectory, respectively. Integer $n$ indicates the $n$th turn and can be written in terms of a floor function "⌊ ⌋" as

$$n=\left\lfloor\frac{\lambda}{2\pi}\right\rfloor+1. \tag{2}$$

Without loss of generality, we have assumed that the turn with $n=0$ in the reverse helical trajectory is a turn in the conventional helical trajectory. For a two-turn reverse helical trajectory specified by $\lambda\in[\lambda_s,\lambda_e]=[-2\pi,2\pi]$, as shown in Fig. 1(a), we have

$$\vec{r}_0(\lambda)=\left(R\cos\lambda,R\sin\lambda,\frac{h}{2\pi}\lambda\right),\quad \lambda\in[-2\pi,0),$$

$$\vec{r}_0(\lambda)=\left(R\cos(-\lambda),R\sin(-\lambda),\frac{h}{2\pi}\lambda\right),\quad \lambda\in[0,2\pi]. \tag{3}$$

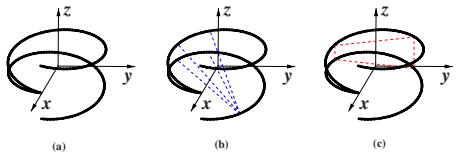


FIG. 1. (a) A two-turn reverse helical trajectory in the coordinate system $\{x,y,z\}$ that is fixed to the imaged object, (b) one-turn and two-turn chords (dotted lines), and (c) a polygon (dotted trapezoid) that is parallel to the $yz$ plane are shown.

We focus only on two-turn reverse helical trajectory in this work, but extension to multiple turns is straightforward. Let $f(\vec{r})$ be an object function with a cylindrical support that is transversely contained within the reverse helical trajectory but extends beyond the reverse helix longitudinally. The cone-beam projection from the source point $\vec{r}_0(\lambda)$ can be written as

$$g(\lambda,\hat{\theta}) = \int_0^\infty dt f(\vec{r}_0(\lambda) + t\hat{\theta}), \tag{4}$$

where $\hat{\theta}$ denotes the direction of x-ray transform of $f(\vec{r})$ from $\vec{r}_0(\lambda)$.

### II.B. First-step (BPF) reconstruction

We first reconstruct the image from the acquired cone-beam data by the use of the chord-based BPF algorithm. Because the reconstruction formula has been explained in detail elsewhere,[10,13] we summarize only briefly the essential steps of the BPF algorithm. A chord can be specified by $\lambda_1$ and $\lambda_2$ on a given source trajectory $\vec{r}_0(\lambda)$. Note that $\lambda_1$ and $\lambda_2$ can be selected from either $[-2\pi,0]$ or $[0,2\pi]$, or from both, where the former chord is referred to as a one-turn chord and the latter chord as a two-turn chord. Example chords are illustrated in Fig. 1(b) as dotted lines. Let $\hat{e}_c$ denote the direction of the chord, and let $x_c$ indicate the coordinate of a point on the chord. The fixed coordinate and the chord coordinate of the point are related through

$$\vec{r} = \tfrac{1}{2}[\vec{r}_0(\lambda_1) + \vec{r}_0(\lambda_2)] + x_c\hat{e}_c, \quad x_c \in [-l,l], \tag{5}$$

where $l = \frac{1}{2}\|\vec{r}_0(\lambda_2) - \vec{r}_0(\lambda_1)\|$ denotes one-half of the chord length. Using $f_c(x_c,\lambda_1,\lambda_2)$ to denote the object function on the chord, we have

$$f(\vec{r}) = f_c(x_c,\lambda_1,\lambda_2), \tag{6}$$

where $\vec{r}$ and $x_c$ are related through Eq. (5).

From cone-beam data $g(\lambda,\hat{\theta})$, one can compute a backprojection image onto the chord as

$$g_B(x_c,\lambda_1,\lambda_2) = \int_{\lambda_1}^{\lambda_2} \frac{d\lambda}{\|\vec{r} - \vec{r}_0(\lambda)\|}\left[\frac{\partial}{\partial\lambda} g(\lambda,\hat{\theta})\right]_{\hat{\theta}}. \tag{7}$$

Based on the backprojection image $g_B$ on the chord, the object function $f_c(x_c,\lambda_1,\lambda_2)$ on the chord is reconstructed by

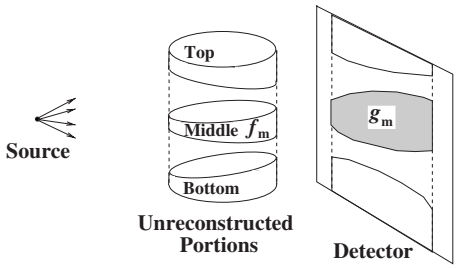


FIG. 2. Schematic of the projection of the unreconstructed portions of the object is shown. $g_m$ represents the projection of the middle portion ($f_m$) of the unreconstructed object.

$$\bar{f}_c(x_c,\lambda_1,\lambda_2) = \frac{1}{2\pi^2}\frac{1}{\sqrt{(x_{c2}-x_c)(x_c-x_{c1})}} \times \left[\int_{x_{c1}}^{x_{c2}} \frac{dx_c'}{x_c - x_c'}\sqrt{(x_{c2}-x_c')(x_c'-x_{c1})} \times g_B(x_c',\lambda_1,\lambda_2) + C\right], \tag{8}$$

with $x_c \in [x_{c1},x_{c2}]$ where $x_{c1}$ and $x_{c2}$ are chosen to cover the object, and the constant $C$ is given by

$$C = 2\pi\int_{x_{c1}}^{x_{c2}} f_c(x_c,\lambda_1,\lambda_2)dx_c = 2\pi g(\lambda_1,\hat{e}_c). \tag{9}$$

Throughout this paper, we will use an upper bar to represent the reconstructed image function. When the detector is large enough to accommodate the projections of all the chords that intersect with the object for a given source position, the BPF algorithm can reconstruct exactly images of the object on the chords. The reconstructed chord images are then converted into Cartesian images by means of interpolation. This volumetric image will contain a middle gap because no chords pass through the gap region.

### II.C. Reprojection and subtraction

Let $\bar{f}(\vec{r})$ denote the volume image reconstructed by the use of the BPF algorithm in the first step. Reprojection of the reconstructed image can be conducted by calculating projections of $\bar{f}(\vec{r})$ for the given scanning geometry as

$$g_r(\lambda,\hat{\theta}) = \int_0^\infty dt\bar{f}(\vec{r}_0(\lambda) + t\hat{\theta}). \tag{10}$$

Subtracting the reprojections from the original projections, one can obtain the projections of the unreconstructed portions of the object as

$$g_s(\lambda,\hat{\theta}) = g(\lambda,\hat{\theta}) - g_r(\lambda,\hat{\theta}) = \int_0^\infty dt\{f(\vec{r}_0(\lambda) + t\hat{\theta}) - \bar{f}(\vec{r}_0(\lambda) + t\hat{\theta})\}. \tag{11}$$

The unreconstructed portions of the object are composed of three distinct portions: Top, middle, and bottom, as shown in Fig. 2. Under the condition that there is no ray passing

through two or more of these portions from any source position, it is feasible to separate the projection of the middle portion from the remaining parts because the supports of the three unreconstructed portions of the object are disconnected in the projection at each view. For given scanning parameters such as the detector size and the source-to-axis distance, the helical pitch can be chosen to satisfy the above condition. Let $f_m(\vec{r})$ denote the middle part of the unreconstructed portions of the object. Its projection $g_m(\lambda,\hat{\theta})$ in Fig. 2 can be written as

$$g_m(\lambda,\hat{\theta}) = \int_0^\infty dt f_m(\vec{r}_0(\lambda) + t\hat{\theta}). \tag{12}$$

### II.D. Second-step (FBP) reconstruction

The second step reconstructs the middle portion of the object, which was not reconstructible by use of the chord-based BPF algorithm, from data $g_m(\lambda,\hat{\theta})$. Consider a polygon plane in Fig. 1(c) that is parallel to the *yz* plane and that intersects the reverse helical trajectory at four distinct points $\vec{r}_0(\lambda_i)$, where $i=1,\ldots,4$ and $-2\pi\leqslant\lambda_1<\lambda_2\cdots<\lambda_4\leqslant 2\pi$. An exact image reconstruction within the polygon for a two-turn reverse helical trajectory can be obtained as[7]

$$\begin{aligned}\bar{f}_m(\vec{r}) &= \frac{1}{2}\sum_{i=1}^{4}\mathcal{K}(\vec{r},\hat{e}_i,\lambda_i,\lambda_{i+1}) \\ &= \frac{1}{2}\sum_{i=1}^{3}\mathcal{K}(\vec{r},\hat{e}_i,\lambda_i,\lambda_{i+1}) - \frac{1}{2}\mathcal{K}(\vec{r},\hat{e}_4,\lambda_1,\lambda_4),\end{aligned} \tag{13}$$

where $\hat{e}_i$ denotes the direction of a polygon side, i.e.,

$$\hat{e}_i = \frac{\vec{r}_0(\lambda_{i+1}) - \vec{r}_0(\lambda_i)}{\|\vec{r}_0(\lambda_{i+1}) - \vec{r}_0(\lambda_i)\|}, \tag{14}$$

where $\lambda_i$ and $\lambda_{i+1}$ denote the starting and ending points of the *i*th subsegment trajectory corresponding to the *i*th side of the polygon, and $i=1,2,3$. For $i=4$, we introduce $\lambda_5$ such that $\vec{r}_0(\lambda_5)=\vec{r}_0(\lambda_1)$. For each of the subsegment trajectories, the Pack–Noo formula provides a reconstruction as

$$\mathcal{K}(\vec{r},\hat{e}_i,\lambda_i,\lambda_{i+1}) = -\frac{1}{2\pi^2}\int_{\lambda_i}^{\lambda_{i+1}} d\lambda \frac{1}{\|\vec{r}-\vec{r}_0(\lambda)\|} g_F(\lambda,\vec{r},\hat{e}_i), \tag{15}$$

where $g_F(\lambda,\vec{r},\hat{e}_i)$ represents the filtered backprojection of the projections of the middle portion of the object, given by

$$g_F(\lambda,\vec{r},\hat{e}_i) = \int_{-\pi}^{\pi} d\gamma \frac{1}{\sin\gamma}\frac{\partial g_m(\lambda,\hat{\theta}(\lambda,\vec{r},\hat{e}_i,\gamma))}{\partial\lambda}, \tag{16}$$

$$\hat{\theta}(\lambda,\vec{r},\hat{e}_i,\gamma) = \cos\gamma\hat{\alpha}(\lambda,\vec{r}) + \sin\gamma\hat{\beta}(\lambda,\vec{r},\hat{e}_i), \tag{17}$$

$$\hat{\beta}(\lambda,\vec{r},\hat{e}_i) = \frac{\hat{e}_i - (\hat{e}_i\cdot\hat{\alpha}(\lambda,\vec{r}))\hat{\alpha}(\lambda,\vec{r})}{\|\hat{e}_i - (\hat{e}_i\cdot\hat{\alpha}(\lambda,\vec{r}))\hat{\alpha}(\lambda,\vec{r})\|}, \tag{18}$$

and

$$\hat{\alpha}(\lambda,\vec{r}) = \frac{\vec{r}-\vec{r}_0(\lambda)}{\|\vec{r}-\vec{r}_0(\lambda)\|}. \tag{19}$$

The integration over $\gamma$ in Eq. (16) indicates a filtering process over the data derivative, while the filtering direction is determined by a preselected unit vector $\hat{e}_i$ specified by Eq. (14) for the corresponding subsegment trajectory. For the imaging problem of practical interest, we show in the Appendix that the intersection of the middle portion of the object $f_m(\vec{r})$ and a polygon plane is enclosed completely within the polygon.

### II.E. Image combination

Finally, combining $\bar{f}(\vec{r})$ and $\bar{f}_m(\vec{r})$ yields the image of the object without a middle gap and without suffering from the long-object data-truncation artifacts. A 3D mask matrix $W_c$, which has digital elements—either 0 or 1—and the same size as the reconstructed images, can be generated so that the voxels intersected by chords have the value of 1 and the others 0. The image combination can then be done by calculating $W_c\cdot\bar{f}(\vec{r})+(\tilde{1}-W_c)\cdot\bar{f}_m(\vec{r})$, where matrix multiplication is defined as element by element multiplication and $\tilde{1}$ represents a 3D matrix of all 1's with the same array size of $W_c$.

### II.F. Use of reduced $\bar{f}(\vec{r})$

Because of the discrete nature of image reconstruction, a seam line artifact at the boundaries of the reconstructed volume images by the two algorithms may occur in the combined images. Let the reconstructed volume image by the chord-based BPF algorithm $\bar{f}(\vec{r})$ be renamed as $\bar{f}_0(\vec{r})$. One can easily create $\bar{f}_1(\vec{r})$ by removing some portion of $\bar{f}_0(\vec{r})$ to ensure that the image reconstructed by the second algorithm, $\bar{f}_m(\vec{r})$, and $\bar{f}_0(\vec{r})$ have overlap regions near the boundaries. Since we know that the polygons always cover more than the middle gap portion of the object image, we can easily find such a reduced volume image $\bar{f}_1(\vec{r})$. Therefore, in the second-step reconstruction, $\bar{f}_1(\vec{r})$ will be used for $\bar{f}(\vec{r})$, and the resulting $\bar{f}_m(\vec{r})$ will be the middle gap portion of $\bar{f}_1(\vec{r})$. Image combination accordingly is given by $W_c\cdot\bar{f}_0(\vec{r})+(\tilde{1}-W_c)\cdot\bar{f}_m(\vec{r})$. The work flow of the proposed tandem approach is summarized in Fig. 3.

## III. NUMERICAL EXPERIMENTS

We perform below numerical studies to demonstrate and validate the proposed method for image reconstruction of a long object from its reverse helical cone-beam data. In the studies, we used the abdomen portion of the NCAT phantom as the imaged object. Currently, the circular trajectory is used for acquiring practical cone-beam data, and the FDK algorithm is used for image reconstruction. Therefore, for comparison, a circular cone-beam scan has also been simulated for which images were reconstructed by use of the FDK algorithm. A virtual, flat panel detector at the isocenter was used in the numerical study. The scanning parameters are

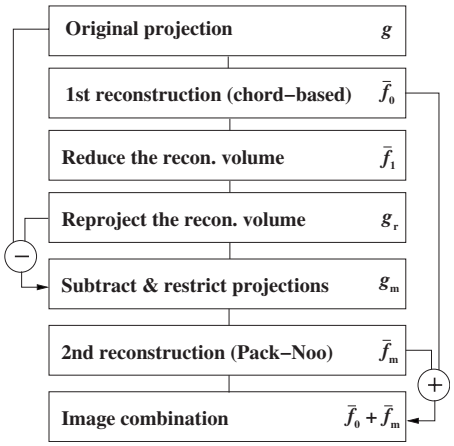


FIG. 3. Flowchart of the proposed tandem algorithm. The chord-based algorithm and the Pack–Noo-formula-based algorithm are used in tandem to reconstruct distinct portions of the object image, and the reconstructed images are combined at the end.

summarized in Table I. Images were reconstructed in $256^3$ cubic voxels with a total side length of 40 cm.

## IV. RESULTS

The simulation results are presented below according to the steps described in Sec. II.

### IV.A. First-step BPF reconstruction

In Fig. 4, we show images $\bar{f}_0(\vec{r})$ reconstructed by using the chord-based BPF algorithm (top row) within 2D slices at (a) $y=0$, (b) $x=0$, and (c) $z=4.375$ cm. Display window of $[0.14, 0.18]$ cm$^{-1}$ is used for all the images throughout this paper unless specified. An off-midplane image is shown in (c) because the midplane belongs to the chordless region. The chordless gap is clearly visualized in the images. For the purpose of preventing a seam line artifact as discussed earlier, rectangular boxes parallel to the $yz$ plane along the $x$ axis have been chosen to extend outside the chordless region by at least one voxel, and the image within each box has been deleted to yield $\bar{f}_1(\vec{r})$ as shown in the bottom row of Fig. 4. For convenience, the heights of the rectangular boxes have been chosen in this example from a linear function of $x$ for $x<0$ and a constant for $x\geqslant 0$ considering the shape of $\bar{f}_0(\vec{r})$.

TABLE I. Scanning parameters used in the numerical study.

| Parameter | Value |
|---|---|
| Source-to-axis distance | 100 cm |
| Source-to-detector (virtual) distance | 100 cm |
| Helical pitch | 20 cm |
| No. of turns | 2 |
| Detector width | 40 cm |
| Detector height | 40 cm |
| Detector array size | 512×512 |
| No. of angular sampling/turn | 1000 |

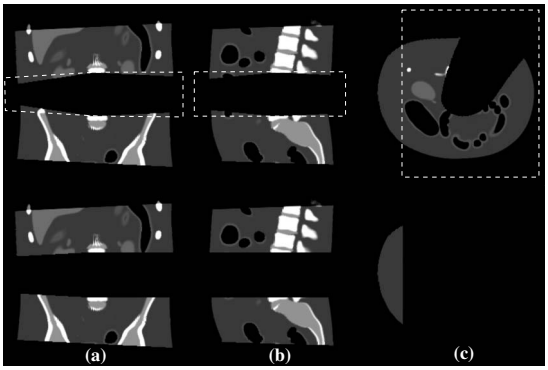


FIG. 4. Slice images of the NCAT phantom at (a) $y=0$, (b) $x=0$, and (c) $z=4.375$ cm reconstructed by the chord-based BPF algorithm (top row). Middle portion bounded by the dotted box was removed to yield the volume image $\bar{f}_1(\vec{r})$ for reprojection (bottom row).

### IV.B. Reprojection and subtraction

In Fig. 5(a), we show the projection of the NCAT phantom at a particular view. Based on the scanning geometry, we reprojected the BPF-reconstructed image $\bar{f}_1(\vec{r})$ to generate $g_r$ shown in Fig. 5(b). A ray-driven line integral has been used for computation of projection and reprojection in this work.[20] The subtracted projection $g_s=g-g_r$ is shown in Fig. 5(c) at the same view as that in Fig. 5(a), and finally the middle portion $g_m$ is obtained by removing the top and bottom data, as shown in Fig. 5(d).

### IV.C. Second-step FBP reconstruction

From the subtracted cone-beam data $g_m$, we use the Pack–Noo-formula-based FBP algorithm to reconstruct the image of the middle-gap region. In Fig. 6, we display the reconstructed images within 2D slices at (a) $y=0$, (b) $x=0$, and (c) $z=0$ cm.

Figure 7 shows the combined images in Figs. 4 and 6. To avoid the seam line artifact, we used the volumetric image $\bar{f}_0(\vec{r})$ reconstructed by the chord-based algorithm in the combination, and the combined images are shown in Fig. 7. To demonstrate the seam line artifact, the combined images of $\bar{f}_1(\vec{r})$ and $\bar{f}_m(\vec{r})$ are presented in Fig. 8.

### IV.D. Noise addition

The two algorithms used in the proposed approach may have different numerical and noise transfer properties, and the reconstructed images from noisy data consequently can

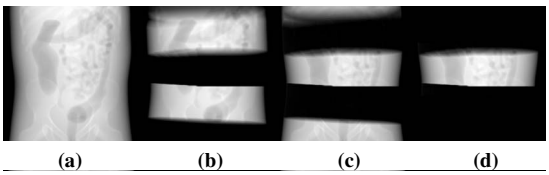


FIG. 5. Projections of (a) the original phantom, (b) the BPF-reconstructed phantom (c) the subtracted projection, and (d) the midportion-only projection.

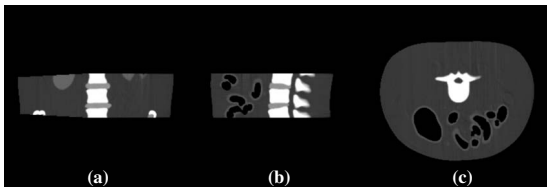


FIG. 6. Slice images of the NCAT phantom at (a) $y=0$, (b) $x=0$, and (c) $z=0$ cm reconstructed by the Pack–Noo-formula-based FBP algorithm.

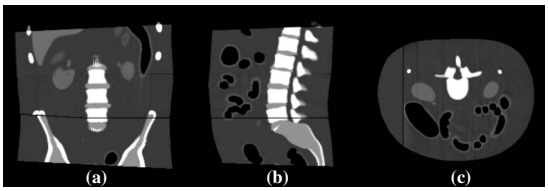


FIG. 8. Slice images of the combination of the reduced, BPF-reconstructed image $\bar{f}_1(\vec{r})$ and the FBP-reconstructed image $\bar{f}_m(\vec{r})$ at (a) $x=0$, (b) $y=0$, and (c) $z=4.375$ cm. The seam line artifacts are observed.

appear differently. We conducted a preliminary simulation study using about 0.25% Gaussian noise in the projection. As can be seen in Fig. 9, the image-noise level in the region reconstructed by the Pack–Noo-formula-based algorithm appears to be higher than that in the region reconstructed by the chord-based algorithm. Although more data are used for the FBP image reconstruction at a point on polygon than those for the BPF at a point on chord, data from the segments of the trajectory constituting sides of the polygon are not redundant with respect to the reconstruction point. Therefore, the data noise propagate additively onto the image noise at the reconstruction point. Note the image noise will be reduced through a weighted averaging when redundant data are summed. Similar noise property and explanation to that can be found in the Ref. 12 for $n\pi$-helical cone-beam CT reconstruction.

### IV.E. Comparison studies

We present below additional images reconstructed by use of the Pack–Noo-formula-based FBP algorithm only and the FDK algorithm for comparison.

#### *IV.E.1. Pack–Noo-formula-based algorithm alone*

Because data filtering occurs in the detector plane, and because the projections of an imaged object may be truncated along some filtering directions, the Pack–Noo-formula-based algorithm can cause truncation artifacts in the reconstructed images if the original projections are directly used. Figure 10 shows the reconstructed images of the NCAT phantom by the use of the Pack–Noo-formula-based algorithm from the original projections. Shading, deformation, and streaks are observed as truncation image artifacts.

#### *IV.E.2. FDK algorithm*

As the motivation of the work was to avoid cone-beam artifacts present in the circular CBCT images, we display for comparison the true phantom images, circular CBCT images reconstructed by the FDK algorithm, and the reverse helical CBCT images reconstructed by the proposed approach in Fig. 11. Line profiles are shown in Fig. 12 for quantitative demonstration of the difference in the images. Intensity drop along the longitudinal direction, streaks, and image deformation are typical circular cone-beam image artifacts;[21–23] streaks and image deformations appear relatively strong, but the intensity drop is not as noticeable partly because of the cylindrical shape, which is relatively uniform along the $z$ axis, of the imaged object.

## V. DISCUSSION

We previously developed an algorithm for image reconstruction from nontruncated data of a short object that is completely within the reverse helix.[7] However, the algorithm cannot be directly used for reconstructing accurate images of a long object that extends out of the polygons for a reverse helical trajectory thereby causing data-truncation problem. Here, we have proposed an image-reconstruction approach for reverse helical CBCT, which is composed of chord-based BPF reconstruction and Pack–Noo-formula-based reconstruction steps in tandem, to address this long object problem. Through numerical studies, the proposed algorithm was validated for accurate image reconstruction of a long object from reverse helical cone-beam data.

In addition to data noise, additional factors can affect the accuracy of the images reconstructed by the proposed approach. In the reprojection step particularly, inconsistency of the data compared to the original projection, which is based on a continuous imaged object, can result from the discretized image and a method for calculation of the line integral such as the ray-driven method. This inconsistency can be minimized by increasing the image-matrix size and improving the line integral computation by averaging more rays

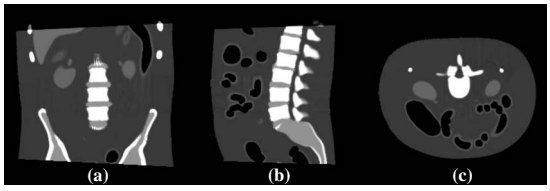


FIG. 7. Slice images of the combination of the BPF-reconstructed image $\bar{f}_0(\vec{r})$ and the FBP-reconstructed image $\bar{f}_m(\vec{r})$ at (a) $x=0$, (b) $y=0$, and (c) $z=4.375$ cm.

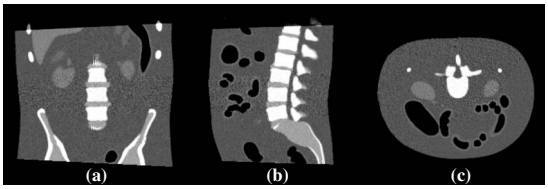


FIG. 9. Slice images of the combined, reconstructed NCAT phantom from 0.25% Gaussian noise in the projection at (a) $y=0$, (b) $x=0$, and (c) $z=4.375$ cm. The display window of $[0.1, 0.256]$ cm$^{-1}$ was used for better visualization.

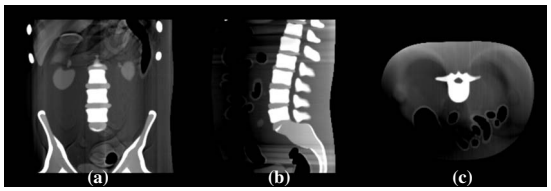


FIG. 10. Slice images of the combined, reconstructed NCAT phantom at (a) $x=0$, (b) $y=0$, and (c) $z=4.375$ cm from the original projections $g$'s.

per detector pixel. Moreover, the data affected by this inconsistency are limited to the projection data corresponding to rays that pass through both the reconstructible and unreconstructible regions of the chord-based BPF algorithm. Physical factors such as scatter and beam hardening can also affect the accuracy of the reprojected data. However, the physical factors can be corrected, we believe, by the use of the existing correction methods.

Although only a two-turn reverse helical trajectory has been studied in this work, it is straightforward to extend this approach for multiple-turn reverse helical CBCT to increase scan volume along the longitudinal direction. The proposed algorithm allows accurate image reconstruction of a long object from reverse helical cone-beam data, and it may be applicable to other scanning configurations such as reduced circular sinusoidal trajectories.[18]

There may be several challenges in the proposed approach for practical applications in IGRT. Imaging radiation dose, although it should be discussed in conjunction with the image quality, can be higher than that from conventional circular scans. Computation time, although we believe is not a real challenge considering recent progress in the accelerated computation techniques such as the graphic-processor-unit acceleration technique,[24] can be relatively more demanding compared to the existing one-shot algorithms for circular CBCT. More investigation is needed on the noise property of the two algorithms in the proposed approach for improving noise uniformity. Methods can be developed to improve the noise characteristics at the algorithm levels such as using data redundancy,[25] and denoising methods may be devised either in a prereconstruction or a postreconstruction fashion to achieve a uniform image noise level between the regions reconstructed by the two algorithms.

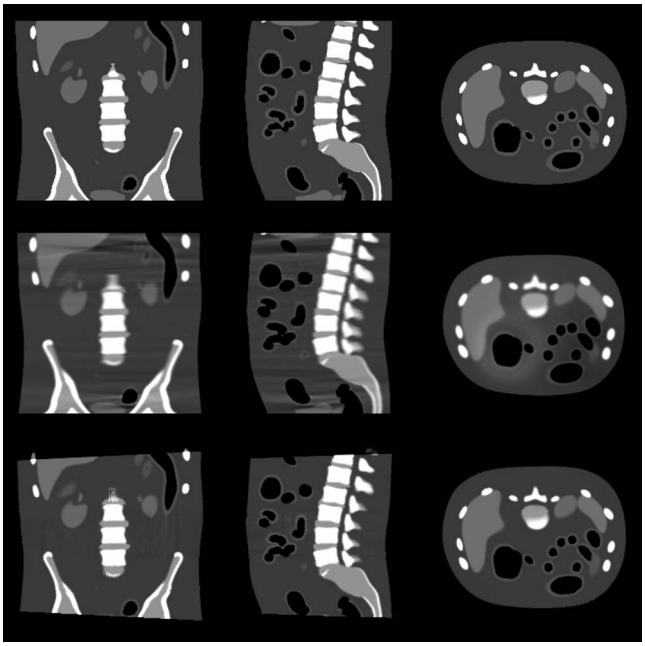

FIG. 11. Slice images at $y=0$ (first column), $x=0$ (second column), and $z=12.8$ (third column) cm of the original NCAT phantom (top row), of the FDK-reconstructed phantom (middle row) and of the tandem algorithm reconstructed phantom (bottom row).

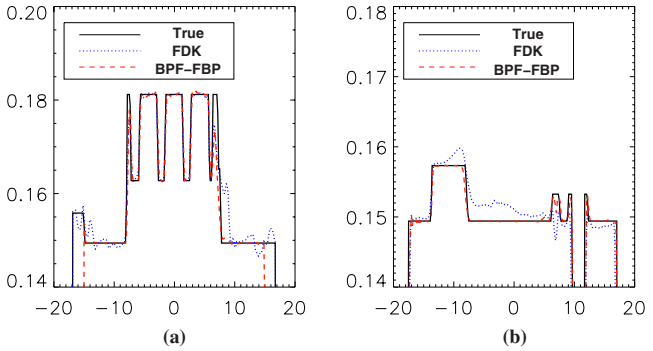


FIG. 12. Line profiles at (a) $x=0$, $y=0$ and at (b) $y=0$, $z=12.8$ cm of the true phantom (solid) of the FDK-reconstructed phantom (dotted) and of the BPF-FBP-reconstructed phantom (dashed).

## ACKNOWLEDGMENTS

The authors would like to thank Dr. W. P. Segars at Duke University for granting the use of the NCAT phantom. One of the authors (S. Cho) was supported in part by a DOD Predoctoral training Grant No. PC061210. This work was also supported in part by National Institutes of Health and Grant Nos. EB00225 and CA120540. The contents of this paper are solely the responsibility of the authors and do not necessarily represent the official views of any of the supporting organizations.

## APPENDIX: POLYGON AND CHORDLESS REGION

We show below that the chordless middle-gap portion of the object is always bounded by polygons that are parallel to the $yz$ plane. Specifically, we assume that the size of the field of view (FOV) is smaller than the polygon widths, which is valid for potential clinical scanning configurations. Considering the symmetry of the trajectory with respect to the $xy$ plane, it is sufficient to show that the reconstructible volume with the top helix (bottom helix) by the chord-based algorithm encloses the top sides (bottom sides) of the polygons. Without loss of generality, we focus on the top helix. For a given polygon parallel to $yz$ plane, we can always find the two vertices on the trajectory, $A$ and $B$, that define the top-side of the polygon, as shown in Fig. 13(a).

We consider a source point $Q_1$ at $\lambda=0$ on the trajectory and possible chords from that point. Because vertices $A$ and $B$ also lie on the trajectory, $\overline{Q_1A}$ and $\overline{Q_1B}$ are also chords. The top helix in Fig. 13(a) is projected to make a concave

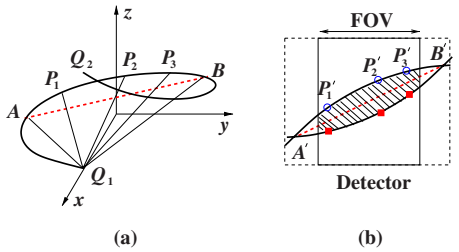


FIG. 13. (a) Schematic of the top helix, the top side of a polygon (dotted line connecting $A$ and $B$), and some chords branching from the point of $\lambda=0$ are shown. (b) Projection of the helix, the top side of the polygon, and the chords on to the detector plane from the source position $Q_1$ and $Q_2$ are shown. We assumed a virtual detector that lies in the polygon plane for illustration here. The points represented by primed letters depict the projection (open circles from the source position $Q_2$, and solid squares from $Q_1$) on to the detector of the unprimed ones in space. The shaded region within the FOV in (b) corresponds to the projection of the reconstructible volume by the chord-based algorithm. The projection of the top side of the polygon is completely enclosed by the shaded region within the FOV. Considering the bottom helix similarly, we can claim the unreconstructible volume by the chord-based algorithm is bounded by the polygon.

curve, as shown in Fig. 13(b). Because of the curvature of the trajectory projection on the detector, the chord-surface is placed beneath the polygon top side.

Now let us consider a source point $Q_2$ at $\lambda=2\pi$ on the trajectory. Similarly, the top helix in Fig. 13(a) is projected to make a convex curve as shown in Fig. 13(b). Because of the curvature of the trajectory projection on the detector, the chord surface is now placed above the polygon top-side. Since the volume between these chord surfaces is completely filled by the additional available chords of the top helix,[10] the top side of the polygon lies within the reconstructible volume by the chord-based algorithm. In other words, the reconstructible region by the chord-based algorithm always extends below the top side of the polygon within the FOV.

By the same token, the bottom side of a polygon lies within the reconstructible volume with the bottom helix by the chord-based algorithm. Therefore, considering both the top and bottom helices, one can claim the chordless middle-gap portion of the reconstructed image by the use of the chord-based BPF algorithm is always bounded by the polygons.

[a]Electronic mail: xpan@uchicago.edu

[1]D. A. Jaffray, "Emergent technologies for 3-dimensional image-guided radiation delivery," Semin. Radiat. Oncol. **15**, 208–216 (2005).
[2]L. Xing, B. Thorndyke, E. Schreibmann, Y. Yang, T.-F. Li, G.-Y. Kim, G. Luxton, and A. Koong, "Overview of image-guided radiation therapy," Med. Dosim. **31**, 91–112 (2006).
[3]J. M. Balter and M. L. Kessler, "Imaging and alignment for image-guided radiation therapy," J. Clin. Oncol. **25**, 931–937 (2007).
[4]L. A. Feldkamp, L. C. Davis, and J. W. Kress, "Practical cone-beam algorithm," J. Opt. Soc. Am. A **1**, 612–619 (1984).
[5]L. E. Court, L. Dong, A. K. Lee, R. Cheung, M. D. Bonnen, J. O'Daniel, H. Wang, R. Mohan, and D. Kuban, "An automatic CT-guided adaptive radiation therapy technique by online modification of multileaf collimator leaf positions for prostate cancer," Int. J. Radiat. Oncol., Biol., Phys. **62**, 154–163 (2005).
[6]S. Yoo and F. Yin, "Dosimetric feasibility of cone-beam CT-based treatment planning compared to CT-based treatment planning," Int. J. Radiat. Oncol., Biol., Phys. **66**, 1553–1561 (2006).
[7]S. Cho, D. Xia, C. A. Pelizzari, and X. Pan, "Exact reconstruction of volumetric images in reverse helical cone-beam CT," Med. Phys. **35**, 3030–3040 (2008).
[8]A. Katsevich, "Theoretically exact FBP-type inversion algorithm for spiral CT," SIAM J. Appl. Math. **62**, 2012–2026 (2002).
[9]A. Katsevich, "An improved exact FBP algorithm for spiral CT," Adv. Appl. Math. **32**, 681–697 (2004).
[10]Y. Zou and X. Pan, "Exact image reconstruction on PI-line from minimum data in helical cone-beam CT," Phys. Med. Biol. **49**, 941–959 (2004).
[11]Y. Zou and X. Pan, "Image reconstruction on PI-lines by use of filtered backprojection in helical cone-beam CT," Phys. Med. Biol. **49**, 2717–2731 (2004).
[12]J. D. Pack, F. Noo, and R. Clackdoyle, "Cone-beam reconstruction using the backprojection of locally filtered projections," IEEE Trans. Med. Imaging **24**, 2317–2336 (2005).
[13]Y. Zou, X. Pan, and E. Y. Sidky, "Theory and algorithms for image reconstruction on chords and within regions of interest," J. Opt. Soc. Am. A **22**, 2372–2384 (2005).
[14]Y. Ye and G. Wang, "Filtered backprojection formula for exact image reconstruction from cone-beam data along a general scanning curve," Med. Phys. **32**, 654–665 (2005).
[15]J. D. Pack and F. Noo, "Cone-beam reconstruction using 1D filtering along the projection of M-lines," Inverse Probl. **21**, 1105–1120 (2005).
[16]J. D. Pack and F. Noo, "Cone-beam reconstruction outside R-lines using the backprojection of 1-D filtered data," Proceedings of the 2005 International Meeting on Fully Three-Dimensional Image Reconstruction in Radiology and Nuclear Medicine, Salt Lake City, UT, 2005, pp. 287–290 (unpublished).
[17]H. Yang, M. Li, K. Koizumi, and H. Kudo, "Exact cone beam reconstruction for a saddle trajectory," Phys. Med. Biol. **51**, 1157–1172 (2006).
[18]D. Xia, S. Cho, and X. Pan, "Image reconstruction in reduced circular sinusoidal cone-beam CT," J. X-Ray Sci. Technol. **17**, 189–205 (2009).
[19]W. P. Segars, "The 4D NCAT phantom," http://dmip.rad.jhmi.edu/people/faculty/Paul/Segars_research.htm.
[20]G. L. Zeng and G. T. Gullberg, "A ray-driven backprojector for backprojection filtering and filtered backprojection algorithms," IEEE Medical Imaging Conference Record, San Francisco, CA, 2003, pp. 1199–1201 (unpublished).
[21]S. Mori, M. Endo, S. Komatsu, S. Kandatsu, T. Yashiro, and M. Baba, "A combination-weighted Feldkamp-based reconstruction algorithm for cone-beam CT," Phys. Med. Biol. **51**, 3953–3965 (2006).
[22]S. Valton, F. Peyrin, and D. Sappey-Marinier, "Analysis of cone-beam artifacts in off-centered circular CT for four reconstruction methods," Int. J. Biomed. Imaging **2006**, 1–8 (2006).
[23]Y. Zou, A. A. Zamyatin, B. S. Chiang, and M. D. Silver, "Reduction of streak artifacts in circular cone beam CT using scanograms," in IEEE Medical Imaging Conference Record, Honolulu, Hawaii, 2007, pp. M18–M294 (unpublished).
[24]F. Xu and K. Mueller, "Real-time 3D computed tomographic reconstruction using commodity graphics hardware," Phys. Med. Biol. **52**, 3405–3419 (2007).
[25]T. Köhler, C. Bontus, and R. Proksa, "BPF reconstruction for helical CT using all data," IEEE NSS-MIC Conference Record, pp. M06–327, 2008 (unpublished).

# Region-of-interest image reconstruction with intensity weighting in circular cone-beam CT for image-guided radiation therapy

Seungryong Cho
*Department of Radiology, University of Chicago, Chicago, Illinois 60637*
*and Department of Radiation and Cellular Oncology, University of Chicago, Chicago, Illinois 60637*

Erik Pearson and Charles A. Pelizzari
*Department of Radiation and Cellular Oncology, University of Chicago, Chicago, Illinois 60637*

Xiaochuan Pan[a)]
*Department of Radiology, University of Chicago, Chicago, Illinois 60637*

(Received 22 August 2008; revised 29 January 2009; accepted for publication 29 January 2009; published 13 March 2009)

Imaging plays a vital role in radiation therapy and with recent advances in technology considerable emphasis has been placed on cone-beam CT (CBCT). Attaching a kV x-ray source and a flat panel detector directly to the linear accelerator gantry has enabled progress in target localization techniques, which can include daily CBCT setup scans for some treatments. However, with an increasing number of CT scans there is also an increasing concern for patient exposure. An intensity-weighted region-of-interest (IWROI) technique, which has the potential to greatly reduce CBCT dose, in conjunction with the chord-based backprojection-filtration (BPF) reconstruction algorithm, has been developed and its feasibility in clinical use is demonstrated in this article. A nonuniform filter is placed in the x-ray beam to create regions of two different beam intensities. In this manner, regions outside the target area can be given a reduced dose but still visualized with a lower contrast to noise ratio. Image artifacts due to transverse data truncation, which would have occurred in conventional reconstruction algorithms, are avoided and image noise levels of the low- and high-intensity regions are well controlled by use of the chord-based BPF reconstruction algorithm. The proposed IWROI technique can play an important role in image-guided radiation therapy.
 [DOI: 10.1118/1.3085825]

Key words: ROI imaging, conebeam CT, chord based reconstruction, IGRT, imaging dose reduction

## I. INTRODUCTION

Cone-beam CT (CBCT) is widely used in image-guided radiation therapy (IGRT) partly due to its rich anatomical information and convenience of use. Target localization is one of the most important steps in IGRT procedures, and a primary reason for using CBCT is to determine the current position of the target and the surrounding normal tissues inside the patient.[1–3] An accurate image of the target is essential for proper target positioning. Uncertainty of the target position requires the use of larger margins in treatment planning which can increase the likelihood of normal tissue complications. Therefore, an accurate image of the target reconstructed by CBCT can improve the chance of favorable patient outcome. The kV cone-beam imaging capability currently available with linear accelerator treatment systems provides excellent soft-tissue contrast and the potential for dose reduction compared to megavoltage (MV) CBCT images, an important benefit in IGRT.

However, total radiation dose to the patient from CBCT imaging prior to each fraction still poses a radiation safety concern.[4] Although the biological effects of imaging radiation dose on the tumor control probability of the target in IGRT require further investigation, it is desirable to spare imaging radiation dose to the normal tissues surrounding the target. Sparing dose to the normal tissues becomes imperative when these tissues are particularly radiation sensitive, such as eyes, breast, or spinal cord. An accurate region-of-interest (ROI) imaging technique in this regard is a potentially important tool for routine CBCT in IGRT. ROI imaging here is used to mean that only the projection of a desired ROI is taken for each view, thereby reducing the dose outside of the ROI. Interestingly, in the report of AAPM Task Group 75, the authors envisioned that a more sophisticated reconstruction technique would be necessary to perform ROI imaging, and thereby reducing imaging radiation dose to the tissues outside the ROI.[4] In this article we report the use of such an advanced reconstruction.

Some of the recently developed image reconstruction algorithms for CBCT can perform certain ROI reconstructions.[5–8] The chord-based backprojection-filtration (BPF) algorithm, for example, can produce accurate ROI images in general CBCT scanning configurations. Data truncation artifacts, often appearing in the reconstructed ROI images using conventional algorithms, can often be avoided by use of the chord-based BPF algorithm. However, for imaging targets located deep within the body the ROI becomes an interior problem, for which no stable, accurate image reconstruction method exists.[9] One approach using the local to-

mography method provides edge-enhanced images from ROI projection data,[10] but this approach does not provide accurate image contrast information which is important in many applications including IGRT.

The proposed intensity-weighted region-of-interest (IWROI) imaging technique can reduce the imaging radiation dose to structures away from the imaging target, while allowing solution of the reconstruction problem by using the chord-based BPF algorithm. We subdivide the reconstructed ROI into inner and outer regions and illuminate the outer region with a filtered beam to decrease exposure during the scan. An intensity-weighting technique has been previously proposed for ROI imaging applications in diagnostics, but only with a conventional reconstruction algorithm which requires nontruncated data for accurate reconstruction.[11–13] A method using two scans, one of which is performed with a full field of view (FOV) and low exposure and the other with a limited FOV and high exposure, has also been studied[14] but this method doubles the acquisition time. Our approach allows some types of data truncation without causing artifacts in the reconstructed ROI image and allows different exposure levels in two sub-ROIs from a single scan. In this work, we focus on circular CBCT, which is the dominant imaging modality employed in most radiation therapy systems, although the method can be extended to general scanning configurations such as the saddle trajectory.

## II. BACKGROUND

The Feldkamp–Davis–Kress (FDK) algorithm is the most widely used algorithm for 3D circular CBCT image reconstruction because of its computational efficiency and acceptable image quality in many applications.[15] However, in the presence of transverse data truncation, the FDK algorithm produces truncation artifacts in the reconstructed images. Since transverse data truncation is common if not unavoidable in ROI imaging, an algorithm that is more robust against transverse data truncation is desirable. The chord-based BPF algorithm is an analytic algorithm that can stably reconstruct ROI images on chords from truncated data. This capability of the BPF algorithm in ROI imaging has been exploited to potentially increase spatial resolution by using a larger geometric magnification in micro-CT applications.[16]

### II.A. Chord-based BPF algorithm for ROI imaging

The chord concept has been developed for exact image reconstruction of a CBCT with general source trajectories; it is rooted in the development of algorithms for helical CBCT. A chord is defined as a line segment connecting any two points on a continuous source trajectory. Specifically, in helical CBCT, a chord connecting two points on the trajectory within one turn is referred to as a PI-line segment. The chord-based BPF algorithm essentially decomposes the image into a number of chords that intersect the imaged object and collectively cover the ROI. The algorithm reconstructs the ROI image along the individual chords. In circular CBCT, since chords can be defined only for the midplane in which the source trajectory resides, virtual source trajectories have been introduced for off midplanes. Additionally, we have introduced virtual chords that connect any two points on the virtual source trajectories. Approximate image reconstruction, therefore, can be performed by use of the BPF algorithm for those off midplanes.[17,18] Derivatives of the cone-beam data acquired by a circular scan are backprojected first onto each chord, followed by the filtering along each chord in one dimension. In the FDK algorithm the filtering occurs in the projection data, thus transverse truncation can produce artifacts in the reconstructed images. In contrast, as long as the imaged object is not truncated along a given chord, the image on the chord can be reconstructed accurately by the chord-based BPF algorithm despite truncations in the projection data. This is the key feature of the chord-based BPF algorithm that enables accurate ROI imaging.

### II.B. IWROI image reconstruction in circular CBCT

In many IGRT applications such as prostate cancer treatment, the imaging target is located deep within the tissue. In this case, we can subdivide the ROI into two regions: inner ROI and outer ROI. The inner ROI can be selected to cover the imaging target, for example, the prostate and nearby organs at risk. The outer ROI would be the remainder of the imaged volume and would include some of the skeletal structures which can be used for image registration. A higher noise level may be tolerable in the outer ROI for skeletal registration as compared to the inner ROI where maximum image quality is required for soft-tissue discrimination. Therefore, we propose to scan the patient with two different levels of exposure: Full exposure to the inner ROI and reduced exposure to the outer. This can be simply implemented using suitable filters in the x-ray beam. Reduced exposure in the outer ROI will decrease the patient dose due to imaging. Additionally the decreased fluence will result in less scatter from the patient's body. Accordingly, the quantum noise

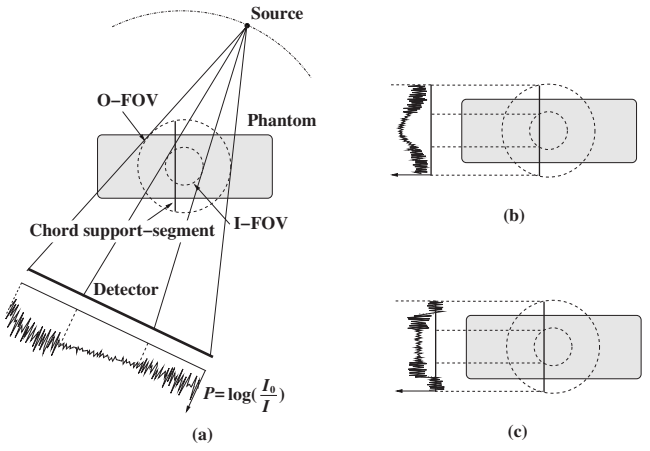


FIG. 1. (a) For each view, the projection data can be separated into two regions having less noise due to higher exposure and vice versa. The noise levels are almost locally confined after (b) backprojecting the data on to a chord support segment and (c) filtration along the chord. Cone-beam data $P$ are calculated from $I_0$ and $I$, which stand for flood field (referred to as open field in this paper) and projection, respectively.

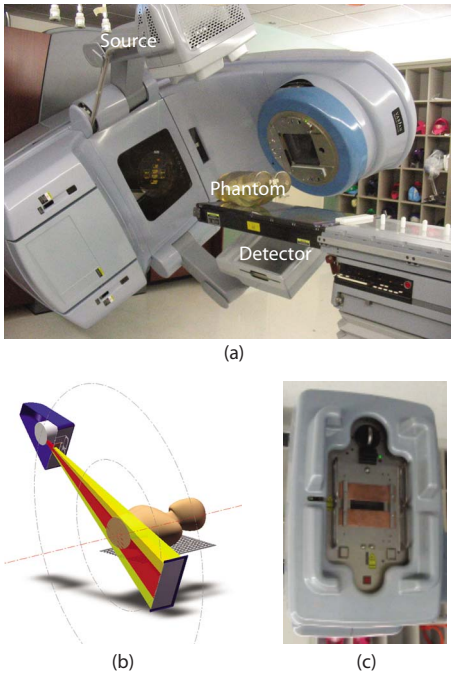


FIG. 2. The OBI system used in the experiment. (a) A picture of the system. (b) Schematic view of the imaging configuration. (c) A picture of the kV source with the IW filters mounted.

level in each projection will be higher in the outer region. Noise properties of the chord-based BPF algorithm have been carefully investigated and it has been shown that the noise of the reconstructed image along a chord is localized in a practical sense.[19,20] This means that the higher noise level in the outer ROI will not substantially affect the noise level in the inner ROI after reconstruction. Figure 1 schematically illustrates the noise propagation in the image reconstruction. Different noise levels in the projection data are merged onto a chord support segment after backprojection, and noise levels remain well separated even after filtration. Numerical simulation studies have successfully verified this noise confinement property of the algorithm in IWROI imaging.[21] The convolution kernel used in the FDK algorithm is also relatively localized, so that the intensity-weighted imaging technique can be utilized with the FDK algorithm in cases where data truncation is negligible or can be compensated for. However, as will be demonstrated, even advanced correction schemes applied in conjunction with FDK cannot correct for large truncations, which may occur for ROI imaging of some anatomical sites.

## III. METHODS

### III.A. System and filters

The imaging work presented here was done with the onboard imaging (OBI) system on a Trilogy linear accelerator (Varian Medical Systems, Palo Alto, CA). The OBI system is composed of an x-ray source and a flat panel detector mounted on the accelerator gantry orthogonal to the treatment beam as shown in Fig. 2. The scanning parameters used in this work are summarized in Table I. A standard clinical scanning protocol with bowtie filter in place uses a beam current 80 mA and a 25 ms pulse. This study removed the bowtie filter leaving portions of the beam completely unfiltered, thus the exposure time was reduced to 13 ms to achieve reasonable intensity levels for open-field images. For reconstruction consistency, acquisition was always performed using a counterclockwise gantry rotation. The field was narrowly collimated in the axial ($y$) direction to minimize scatter effects in the reconstructed image. It was found that even with such a narrow field, scatter is great enough that a scatter correction is required. Four sets of filters were used for the intensity weighting, two each of copper and aluminum. For brevity the filters will be referred to with the following naming convention; Cu1, Cu2, Al1, and Al3 representing 0.32, 0.64, 1.60, and 4.80 cm thicknesses, respectively. These thicknesses were chosen to provide great enough separation of intensity levels in the filtered regions in order to quantify the corresponding changes in image noise. The filters were simple rectangular slabs with square edges and attached to a spare bowtie filter mounting plate.

### III.B. Phantoms

Three different phantoms were used for this study. The first was a solid water (SW) phantom which consisted of $30\times30$ cm$^2$, solid water slabs, commonly available in radiation oncology clinics, stacked 16 cm high. A separate phantom was used for contrast to noise ratio (CNR) measurements, which we refer to as the CNR phantom. This phantom was similarly made from a stack of solid water slabs with a sheet of lucite as a low contrast element and two Teflon rods

TABLE I. System parameters.

| Source | | Detector | | Geometry | |
|---|---|---|---|---|---|
| Parameter | Value | Parameter | Value | Parameter | Value |
| Mode | Full fan | Size_$x$ | 39.73 cm | SAD | 100 cm |
| kVp | 125 kV | Size_$y$ | 29.80 cm | SDD | 149.9 cm |
| mA | 80 mA | Pixel pitch | 194 $\mu$m | Start angle | −182° |
| ms | 13 ms | Pixel matrix | $2048\times1536$ | Stop angle | 178° |
| Collimator_$x$ | ±13.5 cm | Binning | $2\times2$ | No. projections | ~860 |
| Collimator_$y$ | ±3.0 cm | Eff. pixels | $1024\times768$ | | |

as high contrast elements. Finally a pelvis phantom was also imaged, consisting of a partial skeleton ranging from the L1 lumbar vertebra through the mid femur, embedded in lucite formed into a human shaped contour. There were however no soft-tissue inhomogeneities in this phantom.

### III.C. Data corrections

Although the use of IW filters can help decrease scatter in cone-beam projections, the presence of scatter can still be a limitation to image quality and accuracy. Additionally, local variations in beam quality due to hardening by the IW filters can substantially alter the image accuracy; a harder beam lowers the estimated attenuation coefficient. Both of these physical factors, if uncorrected, can degrade image quality. We used a simple, direct method proposed by Siewerdsen *et al.* for scatter estimation.[22] A first-order approximate correction method for the beam-quality effect was used. Note that we use the term "beam-quality effect" rather than "beam hardening" to emphasize that this is not a beam hardening correction as usually understood, which deals with hardening of the beam as it penetrates the patient.

#### *III.C.1. Scatter correction*

The scatter estimation method[22] for cone-beam projections is based on the assumption that the detector signal measured in regions behind the collimator blades is attributable to x-ray scatter. Because the algorithm estimates scatter fluence directly from the projection data, it is robust to a number of variations that exist in cone-beam scans including imaging configuration, patient motion, system geometry, and so on. For each projection we used a second-order polynomial interpolation from the collimator shadows to estimate columnwise scatter fluence. An estimate of the 2D scatter fluence was then obtained by lateral smoothing of the columnwise scatter estimates across all columns. The estimated 2D scatter fluence was subtracted from the original projection, resulting in an estimate of the primary image. Each of the steps in the correction method are illustrated in Fig. 3.

#### *III.C.2. Heterogeneous beam-quality correction*

The reconstruction process involves transformations of the cone-beam data (represented as $P$ in Fig. 1) rather than the raw projection data. The cone-beam data ideally represent the integrated attenuation along each ray. For the present study, this was calculated as the natural logarithm of the ratio of the open field intensity map to the acquired projection. The open field intensity was measured by taking a repeat scan with the same x-ray technique, geometric parameters, and filters in place, but the couch and phantom removed from the field of view. The division process in calculating $P$ should normalize out the reduced beam intensity of the filtered region. However, since this beam has been hardened by the filter, the computed attenuation values will be lower than in the unfiltered region. In order to increase the accuracy of the image values in the filtered region and increase value consistency with the unfiltered region, a simple first-order approximate correction scheme was applied. The assumption was made that the energy spectra of the beams could be represented by single average energies. Additionally, the assumption was made that the ratio of linear attenuation coefficients for the two energies was similar to that of water, for all imaged materials. The second assumption is expected to be valid for air, water, and muscle in the x-ray energy range used in this work, but to slightly underestimate the ratio for bone. Following this assumption, the beam-quality correction was performed by simply multiplying the cone-beam data ($P$) under the IW filter by the estimated ratio of attenuation coefficients without and with the filter. This was estimated from the anterior-posterior (AP) projection of the solid water phantom, where there was an almost uniform thickness of uniform material for both filtered and unfiltered rays. Variation in the thickness due to obliquity was computed to have less than 0.2% effect on the reconstructed image. The square edges of the IW filters resulted in a geometric penumbra region in the projection image, and interpolated ratio values were used in this transition region.

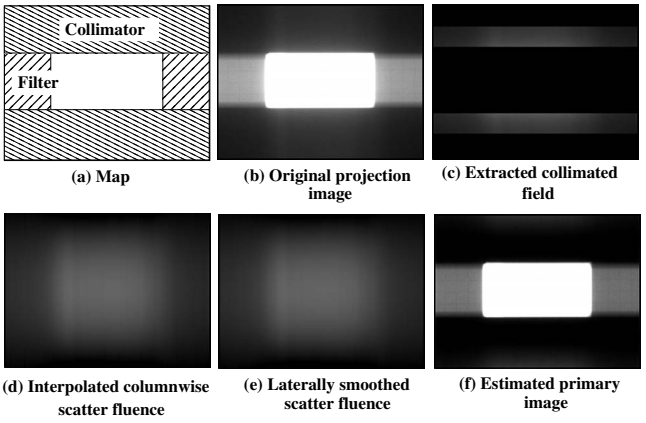


FIG. 3. Scatter correction procedure is illustrated with example images. (a) The collimators and the IW filters are positioned. (b) Original projection image of a phantom. (c) Projection data under the collimators are extracted. (d) Column wise interpolation is applied for each column. (e) Lateral smoothing is performed to finally estimate the scatter fluence. (f) Original image subtracted by the estimated scatter fluence.

## IV. RESULTS

### IV.A. Data corrections

All of the results presented in the following sections are based on corrected data, where the scatter correction and the beam-quality correction have both been applied to the projection data. Unless otherwise noted, the boundary between the inner and outer regions can be visualized in the images as the prominent ring due to the sharp transition in intensity which has not yet been corrected for. All images presented here represent the reconstructed region based on a rectangular parallel chord set that fits the FOV as shown in Fig. 4, and the object extending beyond the FOV (indicated by the outer dashed ring) had been truncated.

Examples of uncorrected and partially corrected data are shown to visualize the effects of data corrections in this sec-

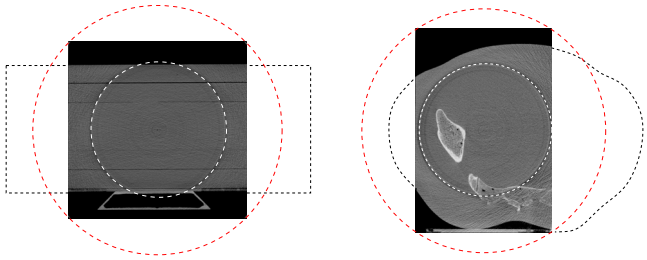


FIG. 4. Transverse slice images of the reconstructed phantoms to illustrate the inner and outer rings that define filtered zone and the full extent of the illumination, respectively. Approximate outlines of the phantoms have also been included to help visualize the scanning configuration in (a) SW phantom or CNR phantom (SW shown) and (b) pelvis phantom.

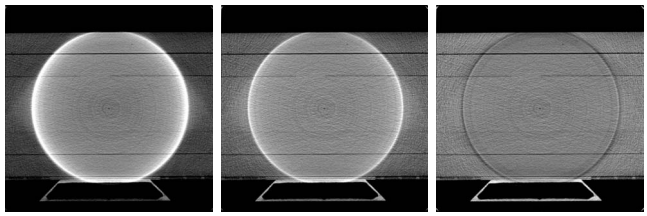


FIG. 5. Transverse slice images of the reconstructed SW-phantom scanned with Cu1 filter are displayed: (a) No correction, (b) scatter correction, and (c) scatter+beam-quality correction have been applied. Display window is $[0.1,0.3]$ cm$^{-1}$. Inner and outer ROIs can be easily distinguished by the pronounced ring artifact in this figure and in all the following figures.

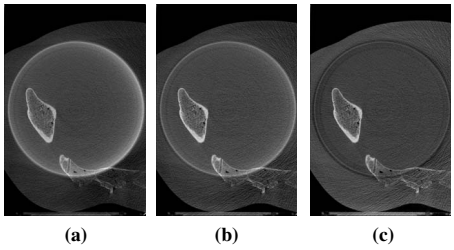


FIG. 6. Transverse slice images of the reconstructed pelvis phantom scanned with Cu1 filter are displayed: (a) No correction, (b) scatter correction, and (c) scatter+beam-quality correction have been applied. Display window is $[0.1,0.6]$ cm$^{-1}$.

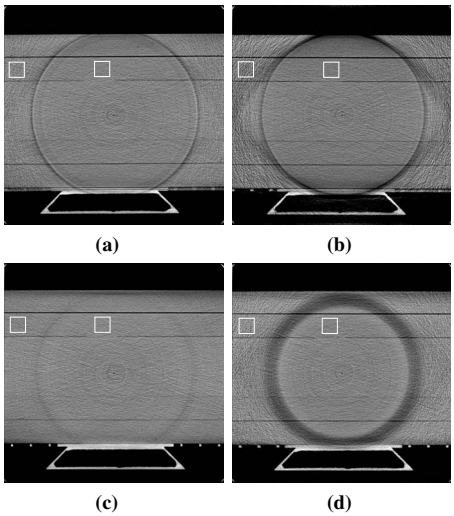


FIG. 7. Transverse slice images of the reconstructed SW-phantom scanned with (a) Cu1 filter, (b) Cu2 filter, (c) Al1 filter, and (d) Al3 filter. Display window is $[0.1,0.3]$ cm$^{-1}$.

TABLE II. Noise levels (coefficients of variation) measured in inner and outer ROIs of the SW phantom.

| | Inner (%) | Outer (%) |
|---|---|---|
| Cu1 | 5.1 | 8.3 |
| Cu2 | 5.0 | 14.5 |
| Al1 | 4.9 | 6.1 |
| Al3 | 5.3 | 9.8 |

tion. In Fig. 5 we display reconstructed images of the SW-phantom scanned with the Cu1 filter (a) before any correction, (b) after scatter correction, and (c) after scatter and beam-quality correction. A cupping artifact due to scatter is observed in Fig. 5(a) and is suppressed substantially after the scatter correction is applied, as shown in (b). Image uniformity is recovered after beam-quality correction (c). The same correction parameters have been applied in the pelvis phantom scan to see the correction effects for a more realistic case, and the results are displayed in Fig. 6.

### IV.B. Noise study

A noise evaluation study was performed with the SW phantom for each of the four different filters (see Fig. 7). Small square regions were selected from each image within the inner and outer ROIs for statistical analysis. Coefficients of variation (standard deviation divided by the mean value) were computed and the results are summarized in Table II.

### IV.C. CNR study

Similarly, a CNR evaluation study was performed with the CNR phantom for each of the four filters. Eight small rectangular regions were selected from each image, four each in the inner and outer regions, positioned within the contrast media and nearby solid water background. The upper pairs in the images in Fig. 8 were used for the calculation of the contrast to noise ratio in Teflon and the lower set for lucite. For a given contrast material (medium1), e.g., Teflon rod, the adjacent solid water region (medium2) was selected for the CNR calculation. CNR in this study was defined as

$$\mathrm{CNR} = \frac{\mathrm{Mean1} - \mathrm{Mean2}}{(\mathrm{StandDev1} + \mathrm{StandDev2})/2}, \quad (1)$$

where Mean1 and Mean2 stand for the mean values of medium1 and medium2, and StandDev1 and StandDev2 represent the standard deviations of medium1 and medium2, respectively. The results are summarized in Table III.

### IV.D. Pelvis phantom

To test the method in a quasiclinical setting, we used the pelvis phantom. Although it does not have any soft-tissue regions, it contains bony structures that can be assessed qualitatively or quantitatively for further studies such as image registration. Reconstructed images along transverse, coronal, and sagittal planes are shown in Fig. 9 for four IW filters.

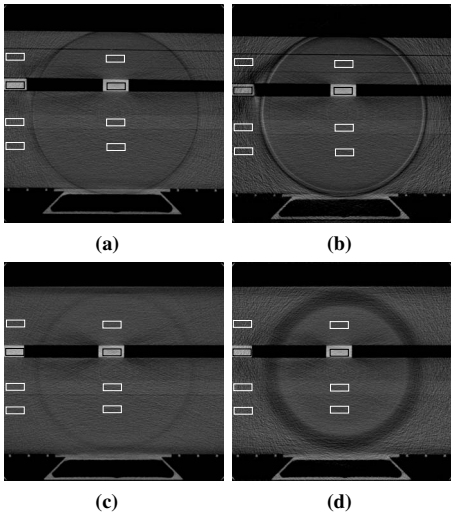


FIG. 8. Transverse slice images of the reconstructed CNR-phantom scanned with (a) Cu1 filter, (b) Cu2 filter, (c) Al1 filter, and (d) Al3 filter. Display window is $[0.1, 0.6]$ cm$^{-1}$.

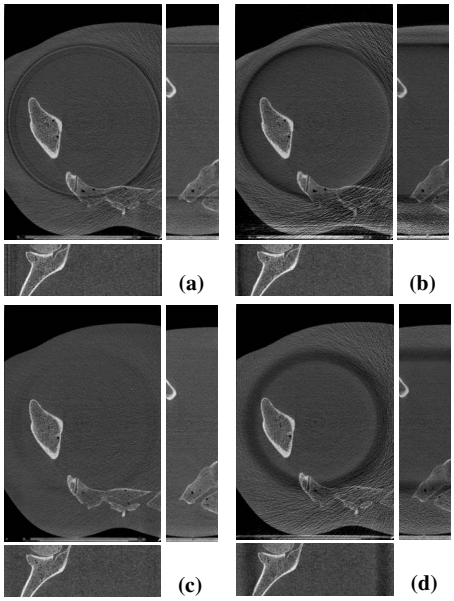


FIG. 9. Slice images—transverse (center), sagittal (right), and coronal (bottom) images—of the reconstructed pelvis phantom scanned with (a) Cu1 filter, (b) Cu2 filter, (c) Al1 filter, and (d) Al3 filter. Display window is $[0.1, 0.6]$ cm$^{-1}$.

## V. DISCUSSION

There have been a number of reported efforts to reduce imaging radiation dose outside a ROI by use of filters. Zonal filters have been used to reduce exposure outside of the windowed region along the longitudinal direction, which does not achieve ROI imaging in transverse planes.[23] ROI filters have also been used for diagnostic purposes such as angiography, head scan, and breast scan.[11–13] However, since only conventional reconstruction based on the FDK algorithm has been employed in these applications, transverse data truncation that can cause image artifacts was minimal or avoided entirely. In contrast, our proposed approach can take advantage of the robustness of the BPF algorithm against transverse data truncation and enables further dose reduction, for some imaging tasks, by reducing the field of view and purposely allowing data truncation.

An example of truncation artifacts is shown in Fig. 10(b), where the same amount of projection data used in our work was used for image reconstruction by the FDK algorithm with the Ram–Lak filter. There exist approximate methods such as data extrapolation for reducing data truncation artifacts, and they may improve the image quality substantially depending on the degree of data truncation in an imaging task. However, because the proposed IWROI imaging technique often involves considerable data truncation, a simple correction scheme such as symmetric mirroring extrapolation[24] may not work as well as in more favorable applications. For example, if a breast is selected as the ROI in breast IGRT, the entire body outside of the breast region will be truncated. Data truncation occurring at highly attenuating materials such as bony structures is also considered hard to compensate for with simple corrections. As shown in Fig. 10(c), a linear extrapolation leads to overcorrection in the pelvis example because the data near one edge of the detector tend to decrease slowly or even increase in some projection angles. Because the convolution kernel in the FDK algorithm has a long negative tail, the extrapolated data in this case contribute to lowering the pixel values after filtering and backprojection. Although it may be possible to devise an approximate correction scheme more appropriate than a simple extrapolation in certain situations, assumptions

TABLE III. CNR measured for high contrast medium (Teflon) and for low contrast medium (Lucite) with respect to solid water in inner and outer ROIs. Contrast and noise are in units of cm$^{-1}$.

| | Teflon | | | | | | Lucite | | | | | |
|---|---|---|---|---|---|---|---|---|---|---|---|---|
| | Inner | | | Outer | | | Inner | | | Outer | | |
| | Contr. | Noise | CNR | Contr. | Noise | CNR | Contr. | Noise | CNR | Contr. | Noise | CNR |
| Cu1 | 0.146 | $1.32\times10^{-2}$ | 11.1 | 0.155 | $1.92\times10^{-2}$ | 8.10 | $1.10\times10^{-2}$ | $1.57\times10^{-2}$ | 0.701 | $1.21\times10^{-2}$ | $1.86\times10^{-2}$ | 0.651 |
| Cu2 | 0.152 | $1.29\times10^{-2}$ | 11.8 | 0.121 | $3.40\times10^{-2}$ | 3.57 | $1.21\times10^{-2}$ | $1.54\times10^{-2}$ | 0.785 | $6.08\times10^{-3}$ | $3.09\times10^{-2}$ | 0.197 |
| Al1 | 0.132 | $1.55\times10^{-2}$ | 8.53 | 0.159 | $1.58\times10^{-2}$ | 10.1 | $1.04\times10^{-2}$ | $1.67\times10^{-2}$ | 0.624 | $1.25\times10^{-2}$ | $1.61\times10^{-2}$ | 0.775 |
| Al3 | 0.144 | $1.53\times10^{-2}$ | 9.46 | 0.139 | $2.87\times10^{-2}$ | 4.84 | $8.57\times10^{-3}$ | $1.48\times10^{-2}$ | 0.579 | $5.89\times10^{-3}$ | $2.75\times10^{-2}$ | 0.214 |

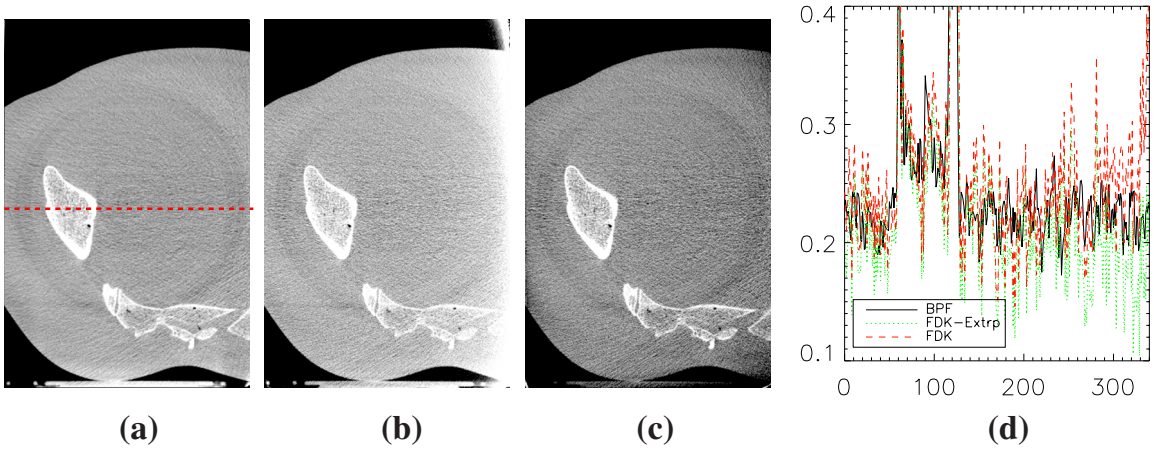


FIG. 10. Truncation artifacts are pronounced in (b) where the FDK algorithm has been used for image reconstruction with the same amount of data that were used in (a) by the chord-based BPF algorithm. The corresponding image reconstructed by the FDK algorithm with a linear extrapolation correction is shown in (c). Display window of $[0.14, 0.32]$ $cm^{-1}$ is used for all images to enhance visualization of the artifacts. Line profiles of the three images along the dashed line shown in (a) are plotted in (d). Solid line represents (a), dashed line (b), and dotted line (c).

of accuracy and robustness against serious data truncation that may arise in a variety of ROI imaging tasks are generally unwarranted. The ring artifacts are more conspicuous in the BPF reconstructed images due to the relatively lower noise background.

The chord-based BPF algorithm in contrast achieves accurate image reconstruction in the face of a large degree of data truncation, which is a fundamental and often important advantage, for example, when CT numbers are to be used as input to radiation transport calculations, or intensity-based segmentation or registration methods. Of course, there may also be situations in which the inaccuracies in FDK reconstructions from truncated data can be acceptable. The accuracy of the chord-based BPF reconstruction has been verified extensively both in numerical and experimental studies.[25,16]

The proposed IWROI technique can achieve more dose reduction than conventional approaches[11–13] without appreciably sacrificing ROI image quality because the robustness to transverse data truncation allows the illuminated region to be further reduced. The zonal filter approach[23] is not directly comparable with the IWROI technique in terms of dose saving because it cannot deal with ROI imaging tasks with transverse data truncations, although it can be considered a synergistic way to improve dose management. A variety of clinical scanning tasks can be performed by use of the IWROI technique, including a breast scan, hemithorax lung scan, extremities, and central-pelvis scan among many others. The potential amount of dose sparing from regional illumination allowed by using BPF reconstruction will be highly task dependent. Typically more superficial sites such as breast, head/neck malignancies, and extremities will see the largest dose sparing. Sites off the central axis of the body may require more advanced hardware for true region of interest illumination but may still benefit significantly. Deep-seated sites may not be spared much dose but this technique with the chord-based reconstruction should perform no worse than if a conventional reconstruction were used.

IW filters are fundamentally different from bowtie filters, which are widely used in clinical systems such as OBI, in that the primary purpose of the bowtie filter is to improve overall image quality.[26] Attenuation of the beam particularly at the peripheral regions of the patient allows the signal intensity to stay within the dynamic range of the detector. Reduced scatter due to attenuation of the beam can also contribute to better image quality. Imaging radiation dose reduction to the patient is an additional advantage of using bowtie filter, although it is not the primary concern. IW filters are introduced to reduce imaging radiation dose to the patient substantially by sacrificing the image quality in selected regions. Therefore the amount of beam filtration from the IW filters is substantially greater than that of the bowtie filters. In order to estimate the amount of beam filtration, exposure was measured with each filter using a Keithley parallel plate ion chamber (75972) and dosimeter (35050A). The results are summarized in Table IV. Although some reduction in exposure has been achieved by the Al1 filter which is close to a conventional bowtie filter in thickness, the ratio of the reduction becomes greater when other filters are used. Scatter -to-primary ratio (SPR) was estimated by use of Siewerdsen's method for AP projection images of the SW phantom for each filter. The computed SPR values from the central region are listed in Table IV as well. It is interesting to note that the results support the fact that the use of bowtie filter, i.e. the IW filters in this case, contributes to

TABLE IV. Exposure was measured ten times at 125 kVp, 80 mA, 65 ms for each case, and average values are listed. SPR is estimated in the middle of AP projections of the SW phantom.

| | Exposure (mR) | Exposure reduction (%) | SPR (%) |
|---|---|---|---|
| No filter | 77.6 | 0 | 11 |
| Al1 | 14.1 | 81.8 | 10 |
| Al3 | 1.74 | 97.8 | 8.3 |
| Cu1 | 2.81 | 96.4 | 9.2 |
| Cu2 | 0.62 | 99.2 | 8.7 |

scatter reduction, although it can be difficult to directly relate the reduction in scatter to the reduction in exposure quantitatively.

Throughout the reconstructed images in the previous section, ring artifacts are pronounced, although the severity varies depending on filter type and thickness. We would like to draw a distinction between the ring artifacts here and the ring artifacts conventionally encountered. Conventional ring artifacts result primarily from nonuniform detector response, which is generally well corrected for in these data. The ring artifacts in this work can be attributed to several factors: inaccurate correction of scatter and heterogeneous beam quality, filter shape, and position, and gravitationally induced pointing errors in the x-ray source. Since our correction methods are approximate and only first order, they may, in fact, amplify data inconsistency resulting in the ring artifacts. Asymmetry of the filter positions in terms of rotation axis would result in a ring-band structure in the images. The aforementioned deficiencies in correction methods and filter position asymmetry are thought to be the primary causes of the thick dropout in the images with Al3 filter. The sharp edges of the filters may also aggravate the effects of the asymmetry and thus increase inconsistency between projection data. Pointing errors and vibration in the source can cause inconsistencies in the transition region that may also increase these artifacts. Accounting for edge effects in the filter design may help minimize the ring artifacts. Pre- or postreconstruction correction algorithms for ring artifacts can be utilized as well, if necessary.[27]

Noise properties of the reconstructed images depend on a number of factors including exposure, electronic noise, energy response of the detector, and reconstruction algorithm. Although more rigorous analysis based on models such as cascaded linear systems of the overall imaging system can help to better understand the image noise, exposure plays a dominant role in determining the noise level of reconstructed images because the imaging system is quantum limited for scanning parameters used in this work.[28] Slightly higher noise in the inner ROI with Al3 filter compared to others is thought to be due to more contamination of the data by scatter from this thick filter. CNR is also related to the factors that affect noise and, in addition, it is susceptible to additional image artifacts such as metal artifacts. Teflon rods create streak patterns around them and degrade image uniformity not only of the rods themselves but also of the neighboring materials. However, inner ROI CNRs of the high contrast material (Teflon) and the low contrast material (Lucite) in solid water are both up to about eight times higher than outer ROI CNRs. Image artifacts are thought to dominate CNR characteristics in Al1-filter case, where an inversion of the expected was observed.

Measurement of the dose reduction by use of the IW filters is in progress and will be reported elsewhere. The influence of image CNR on accuracy of image registration in IGRT must also be investigated so that the proper design of the IW filter can be obtained, for both dose reduction and successful image guidance. Although only a full-fan geometry, where the rotation axis is projected onto the central vertical line of the detector, is assumed in this work, a half-fan geometry in which the rotation axis is projected onto an off-central vertical line of the detector can also be used for the proposed IWROI imaging. The extended FOV of a half-fan geometry can be particularly useful for obese patients.

## VI. SUMMARY

Imaging radiation dose to a patient by repeated CBCT poses a patient radiation safety concern. In this regard, ROI imaging, which limits dose mostly to the imaging target, is desirable. Since ROI imaging of the target in many cases leads to an interior problem, we devised the IWROI method, which illuminates an outer ROI around the target with a reduced fluence, thereby permitting accurate reconstruction. Accurate image information within the inner ROI is maintained as required for tumor localization, whereas relatively poorer image quality in the outer ROI can still result in acceptable image registration in IGRT. The proposed method can reconstruct the target image with high CNR and the surrounding tissue image with a relatively low CNR. Data truncation artifacts can be avoided by using the proposed chord-based BPF-type algorithm, and noise propagation from outer ROI to inner ROI is well suppressed due to the noise properties of this algorithm. We believe the proposed approach is a promising new technique for CBCT in IGRT.

## ACKNOWLEDGMENTS

The authors would like to thank K. Farrey for his help on using the OBI system and Dr. G. Ding at Vanderbilt University for granting the use of the spectrum data of the OBI system. One of the authors (S.C.) is supported in part by a DOD predoctoral training Grant PC061210. One of the authors (E.P.) is supported by NIH predoctoral training Grant T32 EB002103. This work was supported in part by Varian Medical Systems, Palo Alto, CA, and in part by National Institutes of Health under Grant Nos. EB00225 and CA120540. Partial funding for this work was also provided by the NIH S10 RR021039 and P30 CA14599. The contents of this article are solely the responsibility of the authors and do not necessarily represent the official views of any of the supporting organizations.

[a]Electronic mail: xpan@uchicago.edu

[1]D. A. Jaffray, "Emergent technologies for 3-dimensional image-guided radiation delivery," Semin. Radiat. Oncol. **15**, 208–216 (2005).
[2]L. Xing, B. Thorndyke, E. Schreibmann, Y. Yang, T.-F. Li, G.-Y. Kim, G. Luxton, and A. Koong, "Overview of image-guided radiation therapy," Med. Dosim. **31**, 91–112 (2006).
[3]J. M. Balter and M. L. Kessler, "Imaging and alignment for image-guided radiation therapy," J. Clin. Oncol. **25**, 931–937 (2007).
[4]M. J. Murphy, J. Balter, S. Balter, J. A. Bencomo, I. J. Das, S. B. Jiang, C. M. Ma, G. H. Olivera, R. F. Rodebaugh, K. Ruchala, H. Shirato, and F. F. Yin, "The management of imaging dose during image-guided radiotherapy: Report of the AAPM Task Group 75," Med. Phys. **34**, 4041–4063 (2007).
[5]Y. Zou and X. Pan, "Image reconstruction on PI-lines by use of filtered back projection in helical cone-beam CT," Phys. Med. Biol. **49**, 2717–2731 (2004).
[6]Y. Zou, X. Pan, and E. Y. Sidky, "Theory and algorithms for image reconstruction on chords and within regions of interest," J. Opt. Soc. Am. A **22**, 2372–2384 (2005).

[7]F. Noo, R. Clackdoyle, and J. Pack, "A two-step Hilbert transform method for 2D image reconstruction," Phys. Med. Biol. **49**, 3903–3923 (2004).
[8]J. D. Pack and F. Noo, "Cone-beam reconstruction using 1D filtering along the projection of M-lines," Inverse Probl. **21**, 1105–1120 (2005).
[9]F. Natterer, *The Mathematics of Computerized Tomography* (Wiley, New York, 1986).
[10]A. Faridani, D. V. Finch, E. L. Ritman, and K. T. Smith, "Local tomography II," SIAM J. Appl. Math. **57**, 1095–1127 (1997).
[11]R. Chityala, K. R. Hoffmann, D. R. Bednarek, and S. Rudin, "Region of interest (ROI) computed tomography," Proc. SPIE **5368**, 534–541 (2004).
[12]R. Chityala, K. R. Hoffmann, S. Rudin, and D. R. Bednarek, "Region of interest (ROI) computed tomography (CT): Comparison with full field of view (FFOV) and truncated CT for a human head phantom," Proc. SPIE **5745**, 583–590 (2005).
[13]L. Chen, C. C. Shaw, M. C. Altunbas, C.-J. Lai, X. Liu, T. Han, and T. Wang, "Feasibility of volume-of-interest (VOI) scanning technique in cone beam breast CT—A preliminary study," Med. Phys. **35**, 3482–3490 (2008).
[14]D. Letourneau, J. W. Wong, M. Oldham, M. Gulam, L. Watt, D. A. Jaffray, J. H. Siewerdsen, and A. A. Martinez, "Cone-beam CT guided radiation therapy: Technical implementation," Radiother. Oncol. **75**, 279–286 (2005).
[15]L. A. Feldkamp, L. C. Davis, and J. W. Kress, "Practical cone-beam algorithm," J. Opt. Soc. Am. A **1**, 612–619 (1984).
[16]S. Cho, J. Bian, C. A. Pelizzari, C. T. Chen, T. C. He, and X. Pan, "Region-of-interest image reconstruction in circular cone-beam microCT," Med. Phys. **34**, 4923–4933 (2007).
[17]X. Pan, D. Xia, Y. Zou, and L. Yu, "A unified analysis of FBP-based algorithms in helical cone-beam and circular cone- and fan-beam scans," Phys. Med. Biol. **49**, 4349–4369 (2004).
[18]L. Yu, Y. Zou, E. Y. Sidky, and X. Pan, "Region of interest reconstruction from truncated data in circular cone-beam CT," IEEE Trans. Med. Imaging **25**, 869–881 (2006).
[19]D. Xia, L. Yu, E. Sidky, Y. Zou, N. Zuo, and X. Pan, "Noise properties of chord-image reconstruction," IEEE Trans. Med. Imaging **26**, 1328–1344 (2007).
[20]X. Han, D. Xia, E. Y. Sidky, and X. Pan, "Noise properties of the discrete finite Hilbert transform [abstract]. In *IEEE Nuclear Science Symposium and Medical Imaging Conference*," October 19–25 2008, Dresden, Germany: The Nuclear and Plasma Science Society of the Institute of Electrical and Electronic Engineers, M11-5.
[21]S. Cho, E. Pearson, D. Xia, X. Han, C. Pelizzari, and X. Pan, "A preliminary study of intensity-weighted ROI imaging in cone-beam CT," Proc. SPIE **6913**, 69132C (2008).
[22]J. H. Siewerdsen, M. J. Daly, B. Bakhtiar, D. J. Moseley, S. Richard, H. Keller, and D. A. Jaffray, "A simple, direct method for x-ray scatter estimation and correction in digital radiography and cone-beam CT," Med. Phys. **33**, 187–197 (2006).
[23]C. J. Moore, T. E. Marchant, and A. M. Amer, "Cone beam CT with zonal filters for simultaneous dose reduction, improved target contrast and automated set-up in radiotherapy," Phys. Med. Biol. **51**, 2191–2204 (2006).
[24]B. Ohnesorge, T. Flohr, K. Schwarz, J. P. Heiken, and K. T. Bae, "Efficient correction for ct image artifacts caused by objects extending outside the scan field of view," Med. Phys. **27**, 39–46 (2000).
[25]Y. Zou, X. Pan, D. Xia, and G. Wang, "PI-line-based image reconstruction in helical cone-beam computed tomography with a variable pitch," Med. Phys. **32**, 2639–2648 (2005).
[26]S. Yoo and F. Yin, "Dosimetric feasibility of cone-beam CT-based treatment planning compared to CT-based treatment planning," Int. J. Radiat. Oncol., Biol., Phys. **66**, 1553–1561 (2006).
[27]J. Sijbers and A. Postnov, "Reduction of ring artefacts in high resolution micro-CT reconstructions," Phys. Med. Biol. **49**, N247–N253 (2004).
[28]G. X. Ding, M. Duggan, and C. W. Coffrey, "Characteristics of kilovoltage x-ray beams used for cone-beam computed tomography in radiation therapy," Phys. Med. Biol. **52**, 1595–1615 (2007).